

ABSTRACT

SUN, YUJIE. Temperature-dependent Growth Behavior and Mechanical Properties of Atomic Layer Deposited Aluminum Oxide on PA-6. (Under the direction of Dr. Jesse Jur).

Flexible electronic devices based on organic materials are making headway into a variety of new technology areas. To maintain performance in environments containing moisture, atomic layer deposition (ALD) has been used to encapsulate the devices with thin a film barrier. The mechanical properties of these ALD coatings play a key role in the process integration compatibility and long-term reliability of these flexible devices. In this study, nanoindentation characteristics and crack formation of nanoscale ALD alumina on polyamide-6 (PA-6) films was investigated. This work shows that the nucleation behavior of ALD thin films on PA-6 effects at the mechanical performance of the thin films. Initial ALD processing on PA-6 is shown to form a subsurface hybrid layer by reaction between ALD precursors and the polymer backbone, followed by standard Al_2O_3 surface formation in subsequent cycling. Transmission electron microscopy shows that the thickness of hybrid layer decreases with an increase in temperature from 60 to 120 °C. The elastic modulus and hardness evaluated by nanoindentation are shown to an increase with deposition temperatures. The effect of the underlying hybrid layer on the modulus and hardness of ALD thin films was examined and effective mechanical properties of the hybrid layer were estimated. In addition, flexure testing showed that both crack density and critical tensile strain decreased for films processed at lower temperatures that had an increased thickness of the hybrid layer. This work has important consequences in the how ALD materials need to be applied and evaluated on polymers for application as diffusion barrier layers.

© Copyright 2012 by Yujie Sun

All Rights Reserved

Temperature-dependent Growth Behavior and Mechanical Properties of Atomic Layer
Deposited Aluminum Oxide on PA-6

by
Yujie Sun

A thesis submitted to the Graduate Faculty of
North Carolina State University
in partial fulfillment of the
requirements for the Degree of
Master of Science

Textile Engineering

Raleigh, North Carolina

2012

APPROVED BY:

Dr. Wendy E. Krause

Dr. Afsaneh Rabiei

Dr. Jesse S. Jur
(Chair of Advisory Committee)

DEDICATION

This thesis is dedicated to my parents and my sister for their support throughout my life.

BIOGRAPHY

Yujie Sun was born in the small town of Shandong, China. She obtained her Bachelor of Engineering in Textile Engineering, from Donghua University (China) in 2011. In August 2010, she came to North Carolina State University to pursue her Master of Science degree in Textile Engineering. She is planning to pursue a PhD degree after graduating with her M.S. degree.

ACKNOWLEDGMENTS

First and foremost, I would like to thank Dr. Jur for his encouragement, support and guidance during my research. He guided me at every step of the work and gave me the right direction every time I needed. I'm also very grateful to him for giving the opportunity to learn and working in this exciting field.

I greatly appreciate my committee member Dr. Rabiei and Dr. Krause for their interest in my work. I would like to thank Dr. Goertz, Dr. Palmer and Dr. Huang in Sandia National Lab for their help and valuable suggestions during TEM and AFM experiments. I also acknowledge Mangesh Champhekar in Dr. Krause's group for his guidance in the nanoindentation test.

I also thank Department of Textile Engineering, Chemistry & Science, Sandia National Laboratory and Department of Energy for funding this project.

I also would like to express my appreciation to Richard Padbury for his help in TEM and all other group members for their help throughout the project.

I thank my family for their support throughout my life and during my study here from overseas. I'd like to thank my friends for their help in these two years. I would like to give my sincere thanks to Mr. Yao Lu for his encouragement during this time.

TABLE OF CONTENTS

LIST OF TABLES	viii
LIST OF FIGURES	ix
1. INTRODUCTION	1
2. LITERATURE REVIEW	4
2.1 Introduction to ALD	4
2.1.1 Thermal ALD.....	6
2.1.2 Plasma-Enhanced ALD (PEALD).....	8
2.1.3 Applications of ALD.....	10
2.1.4 Comparison to Other Thin Film Process Techniques	12
2.2 ALD on Polymers	14
2.2.1 Growth Mechanisms of ALD Coatings on Polymers	14
2.2.2 Barrier Properties of ALD Coatings on Polymers	17
2.2.3 Other Applications of ALD Coatings on Polymers	19
2.2.4 Comparison to Other Techniques for Inorganic Coatings on Polymers	21
2.3 Mechanical Properties of ALD Coatings.....	23
2.3.1 Fracture Mechanisms of Thin Films	23
2.3.2 Mechanical Properties and Their Test Methods	26
2.3.3. Fracture Behavior of ALD Coatings.....	32
2.3.4 Comparison to Other Deposition Techniques.....	35
3. EXPERIMENTAL.....	37
3.1 Material Preparation.....	37

3.2 ALD Processing	38
3.2.1 ALD Reactor	38
3.2.2 ALD Processing of Alumina.....	39
3.3 Microscopy Characterization Techniques.....	42
3.3.1 Transmission Electron Microscopy (TEM)	42
3.3.2 Atomic Force Microscopy (AFM)	43
3.4 Mechanical Property Characterization Techniques	44
3.4.1 Nanoindentation.....	44
3.4.2 Bending Test	47
4. ALUMINUM OXIDE DEPOSITION ON PA-6.....	48
4.1 TEM Analysis	48
4.2 AFM Analysis.....	53
4.3. Mechanical Analysis.....	58
4.4. Bending Test	66
4.5 Conclusion	71
5. ALUMINUM OXIDE DEPOSITION ON PSR-4000.....	72
5.1 TEM Analysis	72
5.2 AFM Analysis.....	73
5.3 Mechanical Analysis.....	75
5.4 Conclusion	77
6. THESIS SUMMARY	79
7. FUTURE WORK.....	81

8. REFERENCES 82

LIST OF TABLES

Table 1. Elastic modulus and Berkovich hardness of ALD Al ₂ O ₃ coatings	34
Table 2. Mechanical properties of various materials	35
Table 3. Extrapolated contact modulus and hardness, calculated elastic modulus and density of ALD alumina coatings on PA-6.	61

LIST OF FIGURES

Figure 2.1. Schematic diagram of ALD process.....	5
Figure 2.2. Growth model for Al ₂ O ₃ ALD on polymers.....	16
Figure 2.3. Schematic of crack tip field.....	24
Figure 2.4. A two dimensional model of stress distributions in a cracked film.....	26
Figure 2.5. Schematic diagram of (a) sample configuration and (b) holders and bent films on flexible test apparatus.	28
Figure 2.6. (a) A representative load versus indenter displacement curve showing quantities used in an analysis and (b) a representative cross section through an indentation with different quantities.	30
Figure 2.7. Critical tensile strain of different thick Al ₂ O ₃ ALD coatings on different polymers.....	33
Figure 3.1. Thickness of spin cast PA-6 films as a function of spinning speed.	37
Figure 3.2. Schematic diagram of the ALD reactor used in this study.....	39
Figure 3.3. ALD growth per cycle at different temperatures.....	40
Figure 3.4. Temperature window of Al ₂ O ₃ ALD of the reactor used in this study.	41
Figure 3.5. Example curve obtained from nanoindentation of a spun cast PA-6 film.....	45
Figure 3.6. Extrapolation of contact modulus for ALD alumina deposited on PA-6 at 60 °C to zero contact depth.	46
Figure 4.1. Cross sectional TEM images of 100 cycles Al ₂ O ₃ ALD on spun cast PA-6 films at (a) 60 °C, (b) 90 °C and (c) 120 °C.....	49

Figure 4.2. Cross sectional TEM images of PA-6 with 100 cycles Al₂O₃ ALD deposited at 90 °C with different dose time: **(a)** TMA/N₂/H₂O/N₂ = 0.2/30/0.2/45s and **(b)** TMA/N₂/H₂O/N₂ = 2/30/2/30s..... 50

Figure 4.3. **(a)** TEM images of 100 cycles Al₂O₃ ALD on PA-6 films at 60 °C and **(b)** EDX mapping of aluminum and **(c)** gold. **(d)** EDX spectrum image of hybrid layer. 51

Figure 4.4. AFM surface images of **(a)** PA-6 and PA-6 with 100 Al₂O₃ ALD cycles deposited at **(b)** 60 °C, **(c)** 90 °C, and **(d)** 120 °C. 54

Figure 4.5. Circular delamination point on PA-6 films with 100 cycles Al₂O₃ ALD deposited at 60 °C..... 56

Figure 4.6. Magnified AFM images of PA-6 with 100 Al₂O₃ ALD cycles deposited at **(a)** 60 °C, **(b)** 90 °C, and **(c)** 120 °C..... 57

Figure 4.7. AFM surface images of PA-6 with 100 cycles Al₂O₃ ALD deposited at 90 °C using different dose time: **(a)** TMA/N₂/H₂O/N₂ = 0.2/30/0.2/45s and **(b)** TMA/N₂/H₂O/N₂ = 2/30/2/30s..... 58

Figure 4.8. Variation of **(a)** contact modulus and **(b)** hardness vs. contact depth for virgin PA-6 films and PA-6 with 100 cycles Al₂O₃ ALD coatings. **(c)** and **(d)** are the same plots zoomed into 55 nm contact depth. 59

Figure 4.9. Predicted contact modulus for ALD alumina on PA-6..... 63

Figure 4.10. Predicted contact modulus of 100 cycles ALD alumina on PA-6 grown at 60 °C after model adjustment..... 64

Figure 4.11. Load-displacement curve of PA-6 and PA-6 with alumina processed at 60, 90 and 120 °C. 65

Figure 4.12. Representative optical micrographs of the cracked alumina thin films processed at 60 °C **(a)-(c)**, 90 °C **(d)-(f)** and 120 °C **(g)-(i)** for 200 cycles..... 67

Figure 4.13. Crack initiating critical strain of 200 cycles alumina films processed at 60, 90 and 120 °C. 68

Figure 4.14. **(a)** Crack spacing and **(b)** crack density vs. tensile strain on the top of the bending curvature for 200 cycles alumina films processed at 60, 90 and 120 °C..... 69

Figure 5.1. Cross sectional TEM images of 100 cycles Al₂O₃ ALD on PSR-4000 sheets at **(a)** 60 °C, **(b)** 90 °C and **(c)** 120 °C. The higher resolution images **(d)-(f)** show the microstructure of the alumina coating..... 72

Figure 5.2. AFM surface images of **(a)** PSR-4000 and PSR-4000 with 100 Al₂O₃ ALD cycles deposited at **(b)** 60 °C, **(c)** 90 °C, and **(d)** 120 °C. 74

Figure 5.3. **(a)** AFM height image and **(b)** AFM phase image of PSR-4000 with 100 Al₂O₃ ALD cycles deposited at 60 °C. 75

Figure 5.4. Variation of **(a)** contact modulus and **(b)** hardness against the contact depth for PSR-4000 and PSR-4000 with 100 cycles ALD alumina coatings grown under 60, 90 and 120 °C..... 76

1. INTRODUCTION

Flexible electronic devices have been adopted in various technology areas, including displays, lighting, photovoltaic, and integrated circuits, attributing to their mechanical flexibility and large area processing compatibility.[1] As most of the flexible devices are based on polymer substrate, they will show degraded performance when exposed to moisture and oxygen in environment. Encapsulation to devices is required for long term operation. A traditional encapsulation method is to seal the device in an inert gas using a metal or glass lid.[2] This method sacrifices the flexibility of the device. Alternatively, nanoscale thin-film encapsulation can be used that offer good flexibility. The thin film barriers can be formed from Al, Al oxide or Si oxide by means of evaporation, sputtering and plasma-enhanced chemical vapor deposition (PECVD). Recent interest is turning to the use of atomic layer deposition (ALD).

ALD is an attractive thin film deposition technique due to its self-limitation reaction process to form conformal, pinhole free inorganic thin films at low temperatures.[3, 4] It is a common method to design the ALD process by pumping two reactants in an alternating fashion, and using nonreactive gases to purge the excess precursor each time after the surface reaction has reached completion.[5] ALD provides the capabilities for producing oxides, nitrides, and metals.[3] ALD was initially developed to produce thin film electroluminescent (TFEL) displays[6] and now its application has been extended to applications such as modification of surface characteristics, insulators for microelectronics, transparent conductors, optical coatings and protecting barriers. [7-10]

Since ALD materials growth can occur at low temperature (<150 °C), there is great interest to examine the growth of ALD thin coatings on polymers. In general, nucleation behavior of ALD on polymers can be categorized in three mechanisms: [11, 12]

- 1) For polymers with reactive sites on the surface, like cotton, the precursors can react with the functional groups and form an abrupt layer on the surface, much like ALD growth on inorganic surfaces. The growth rate of the ALD thin coating is almost independent of the deposition temperature within the ALD temperature window.
- 2) For polymers with a nonreactive surface, the precursors will diffuse into the polymer and nucleate in the subsurface. This process is greatly affected by the temperature. Transmission electron microscope images of polypropylene (an inert polymer) with ALD alumina coatings processed at different temperatures demonstrate that higher process temperatures lead to substantial subsurface growth. This is ascribed to polymer expansion at high temperature which increased diffusion of precursors into the polymer.[12]
- 3) In the third type, the precursors are allowed to diffuse into the polymer and subsequently react with its functional groups, forming a hybrid layer between the coating and substrate. This work investigates the mechanical properties of this third type of ALD materials growth on polymers and attempts to elucidate effect of the hybrid layer on these properties.

The mechanical behavior of ALD thin film coatings on hard inorganic substrates has been widely studied using nanoindentation, a popular technique to determine modulus and

hardness of a thin film.[13-16] During the nanoindentation process, the instrument can record the penetration depth of tip into the samples as the load increases at a constant rate, therefore forming the relationship between the load and depth. A common method for analysis is presented by Oliver and Pharr,[16] which requires that when measuring a coating/substrate system, the indentation depth must be limited to less than 10% of the film thickness in order to get 'film only' properties.[17] Few studies have investigated the mechanical properties of nanoscale ALD coatings on soft polymer materials. This work explores the use of nanoindentation to determine the mechanical properties of nanoscale ALD coatings. This work, therefore, plays an important role in understanding the long-term reliability of ALD thin coating application as a barrier layers for flexible devices.

In this study, the nanoindentation characteristics and flexural behavior of ALD alumina on PA-6 and PSR-4000 grown under different temperatures are determined. PA-6 is a representative polymer on which the ALD process follows the third type growth mechanism, forming a hybrid (inorganic-organic) subsurface layer.[11] PSR-4000 has been used as the solder mask for flexible printed circuit boards and ALD growth mechanisms on this material are unknown to this point. TEM was used to observe the temperature influence on the growth behavior of ALD alumina coatings. The change to surface microstructure of the polymers after ALD coating was observed using AFM. Nanoindentation was used to evaluate the modulus and hardness of the ALD alumina coating on polymers. Effect of hybrid layer on modulus and hardness of the coating was determined by comparing the measured result with predicted value obtained using a literature model.[18] Flexibility of the coating on free-standing PA-6 was also detected through a custom bending apparatus.

2. LITERATURE REVIEW

2.1 Introduction to ALD

Atomic layer deposition (ALD) is a self-terminating surface reaction process. It was first demonstrated by Dr. Suntola with the growth of ZnS film.[6, 19] As shown in Figure 2.1, the process generally includes four separated steps: (1) adsorption of one precursor onto the substrate surface; (2) purging the excess precursor and by-products out of the reactor using nitrogen or argon; (3) self-limiting reaction of the second precursor, activating the surface again for the reaction with the first precursor; (4) purging the redundant precursor and by-products.[3] To make sure effective entrainment to reactants and purging from stagnant gas, the optimum pressure of carrier gas was determined to be around 1 Torr.[5] If the pressure is higher, the interdiffusion coefficient of gas in N_2 is smaller, leading to harder removal of reactants and by-products from stagnant gas in the reactor. Longer purge time will be needed. If the pressure is too low, the mean free path of N_2 is too long to provide effective entrainment to the reactant. Thus the inert carrier gas pressure of 1 Torr is a trade-off between these two factors.

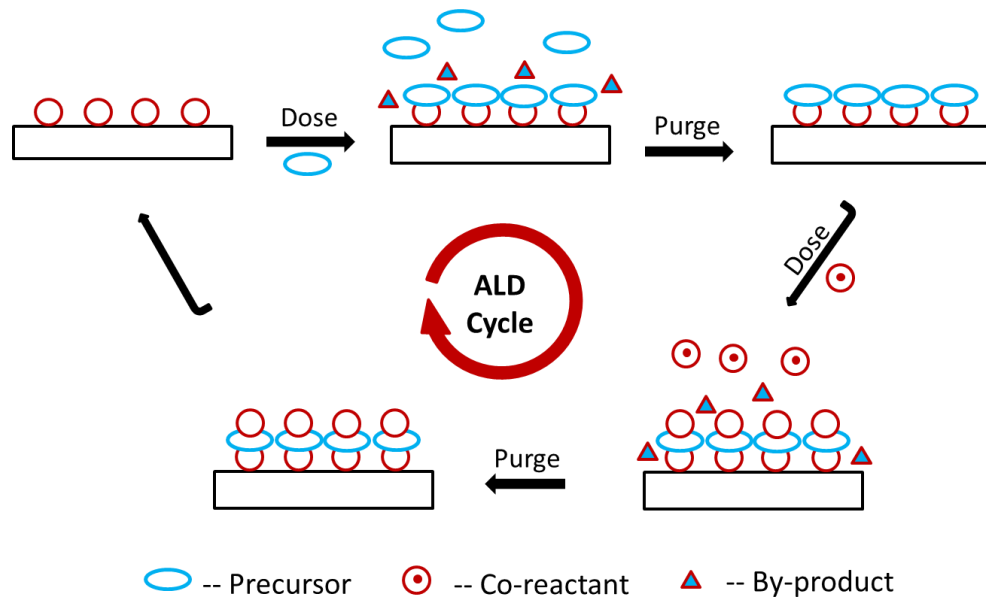


Figure 2.1. Schematic diagram of ALD process using self-limiting surface chemistry and ABAB binary reaction sequence.

After one sequence, one atomic layer of materials can be formed on the substrate, and through repeating the sequence, the films will grow layer-by-layer. As the precursor gas molecules can reach each site of the surface, the coating achieved through ALD is pinhole free and conformal to the original substrate regardless of the aspect ratio of the structure, making the ALD process satisfying to modern thin film deposition with precise thickness control.[5]

A wide selection of metals and metal oxides thin films have been deposited successfully using ALD. Although it was initially applied for electronic materials, the ALD process has begun to be used to modify the properties of biomaterials,[7, 8] organic polymers,[20] inorganic membranes[21] and textiles with complex geometries[22]. For example, ALD has

been shown to change the wettability of nonwoven polypropylene and cotton fabrics.[22] These properties show particular application in functional fiber-based system. Another important application of ALD coating is as a gas-diffusion barrier for biomaterials,[8] packaging materials[10] and flexible electrical devices[23-25]. For example, Carcia et al. [23] estimated that a 25nm thick ALD Al₂O₃ film on poly(ethylene naphthalate) had a water vapor transmission rate about 6×10^{-6} g/m²/day. Further improvements were achieved when the ALD alumina films were combined with other inorganic or organic layers.[2, 24, 25]

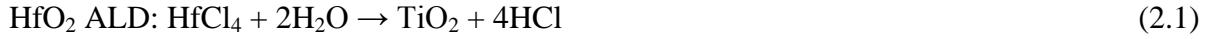
In general two types of ALD process exist: i) thermal ALD and ii) plasma enhanced ALD. These processes will be detailed in the following sections.

2.1.1 Thermal ALD

ALD reactions that occur without the help of plasma or radicals are referred to as thermal ALD. There is a deposition temperature window for thermal ALD to obtain ALD growth in a constant rate. If the temperature is too high, precursors may decompose and allow additional reactant adsorption. Or the density of reactive site will be reduced, leading to lower deposition rate. If the temperature is too low, precursors will condense onto the substrate surface, increasing deposition rate. When the deposition temperature is increased from low to high, the deposition rate can maintain constant in a range.

Thermal ALD reaction is closely related to chemical vapor deposition (CVD).[5] For CVD based on binary reactions, the two reactants are pulsed into the reactor at the same time. In ALD, the substrate is exposed to the reactants in a stepwise fashion. It is a common method to design the ALD process by pumping the two reactants used in CVD separately, and using

inert gases to purge the excess precursor each time after the surface reaction has reached completion. HfO₂, [26] TiO₂ [27] and ZnO [28] ALD are all resulted from the binary reaction CVD processes. Their reactions are as follows:



One of the most common ALD models is thermal Al₂O₃ ALD because of favorable reaction energies. This reaction has an extremely high reaction enthalpy, up to 376 kcal. [5] Trimethylaluminum (TMA), aluminum trichloride or dimethylaluminum chloride (DMACl) can be used as metal precursor to provide Al atom for the coating, while H₂O, H₂O₂ or O₂ is used to react with ligands of precursors. [29] The TMA and water process is most widely used. The reaction mechanism can be described as: [19, 30, 31]



where the asterisks represent reaction site on the surface. Typical growth rate for ALD Al₂O₃ is 1.1-1.2Å per cycle. As the distance of hexagonally close-packed oxygen planes in sapphire is 2.17Å, it means that approximate half a monolayer of Al₂O₃ is deposited per cycle. [32] Alternating exposure to TMA and water results in the Al₂O₃ growth layer-by-layer on the substrate. The obtained amorphous ALD Al₂O₃ film has a density of 3.5 g/cm³ when the deposition temperature is 450K and the refractive index is 1.65 ± 0.02. [31]

Earlier studies of thermal ALD are usually proceed under high temperature ranging from 100 to 500 °C or above [29, 31-33]. This temperature is not suitable for thermally constrained materials such as polymers and biomaterials. To expand the application of thermal ALD to those materials, ALD at temperature less than 100 °C has been explored. For example, low temperature deposited Al₂O₃[4] and ZnO[34] have been studied in recent years for application on flexible electronic devices. It was found that the Al₂O₃ film have lower densities at low deposition temperature, which was explained by high hydration concentration in the film. Low surface roughness and good electrical properties are also observed on Al₂O₃ ALD films grown under low deposition temperature.[4] Due to the low kinetics of precursor at low temperature, the purge time needs to be prolonged to 180 seconds when the deposition temperature is 33 °C.[4]

2.1.2 Plasma-Enhanced ALD (PEALD)

Some single element metal films are very difficult to deposit using thermal ALD process.[35] Fortunately, these elements can be deposited using plasma or radical-enhanced ALD. The plasma source can generate reducing agent or other energetic species to reduce the required growth temperature and induce needed reactions.[5] Hydrogen radical is commonly used reducing agent. For example, a reaction process of TaCl₅ and hydrogen radicals for the formation of Ta can be expressed as:[5]



TaCl₅ and hydrogen radicals are two precursors used in this process. The asterisks represent reactive sites on the surface of substrates.

The plasma used in a PEALD can be generated by radio frequency, microwave and electron cyclotron resonance (ECR).[35] In a PEALD chamber, there is always a RF coil to generate plasma above the substrate.

In general, the PEALD produces better quality films at lower deposition temperature because the plasma can provide the activation energy to the reaction.[35] For example, Ta CVD by thermal deposition of Ta halides can only proceed at temperature approximately 2000°C, while PEALD using TaCl₅ and atomic hydrogen can reduce deposition temperature as low as 150°C.[36] Good quality Ta thin films with low Cl concentration have been grown on Si and SiO₂ substrates at that temperature. Ruthenium and cobalt thin films obtained by NH₃ PEALD have also been reported to have better quality than thermal ALD films.[37, 38] A drawback of PEALD is that the deposited films was non-conformal to the substrate when using trenched samples with a high aspect ratio, [39]. The thickness of film at the top of the trench was 28nm, while the film at the bottom of the trench was only 11nm. The non-conformal coatings limit the use of radical-enhanced ALD in coating of substrates with a very high aspect ratio.

Other than the metal, single element semiconductor such as Si and Ge can also obtained using PEALD [5]. The surface chemistry for Si ALD using hydrogen radicals is shown in the following:





At appropriate temperatures, hydrogen radicals will activate the Si surface to make it reactive with SiH_2Cl_2 . The hydrogen radicals also add hydrogen atoms to surface chlorine or hydrogen to produce HCl or H_2 which will be removed by the hydrogen radicals eventually.

PEALD can also be used to deposit compound materials, such as the oxides formed via thermal ALD. PEALD can extend the temperature window to room temperature, making the temperature window much wider than that of thermal ALD. For example, the use of O_2 plasma radicals in Al_2O_3 PEALD enables deposition at room temperature, leading to the process promising for manufacture of barrier layers on polymer substrates.[40, 41] The reactions between $-\text{CH}_3$ ligands and O_2 radicals are similar to combustion reaction which can produce H_2O and CO_2 . The H_2O will lead to thermal-ALD-like reaction and form $-\text{OH}$ surface for chemisorption of $\text{Al}(\text{CH}_3)_3$. [40] The growth rate of alumina using $\text{Al}(\text{CH}_3)_3$ and O_2 plasma at room temperature is about $1.7 \text{ \AA}/\text{cycle}$. Compared to a growth rate of $1.2 \text{ \AA}/\text{cycle}$ for thermal ALD, the increased growth rate has been attributed to a higher number of reactive groups created by O_2 plasma for chemisorption of metal organic precursor.

2.1.3 Applications of ALD

ALD was originally developed by Suntola and his co-workers to produce thin film electroluminescent (TFEL) displays.[6] In early work, ALD materials were shown to work very well as phosphor and insulators in TFEL displays. The benefit of ALD was that you could achieve the thickness required in a simple and concise way, and the three layers system could be manufactured in a single ALD processing sequence.[9] In addition, doping of ALD

materials produced the most efficient TFEL phosphor, ZnS:Mn, of which the emission band is so broad that it can be used as a red or green phosphor with proper filters. Here doping is achieved by intermittently replacing a zinc precursor pulse with manganese precursor pulses.

The ALD process is also used to producing the insulators for microelectronics or nanoelectronics as the present and future integrated circuit require much thinner films with precise thickness control.[9] High- κ dielectric materials are required with further shrinkage of modern transistors, to replace the silicon dioxide or nitride silicon dioxide, of which the current leakage increases with the decrease of thickness. ALD is also an ideal method to produce the high efficient transparent conducting oxides. The pin-hole free and dense structures of ALD coatings make them suitable as the passivating and protecting layers, especially on polymer substrates, attributing to its low processing temperature. Transition metal nitride diffusion barriers are used in integrated circuit to prevent the inter-diffusion of metals and insulators. They are required to be pinhole free, thin and conformal to substrate with high aspect ratio. Thus, the use of ALD is favored in the production of transition metal nitride diffusion barriers.

ALD processing has been used to produce the thin metal films. To get uniform metal films through ALD, the reducing agent and metal precursor must be chosen to make sure the byproducts won't etch the metal films and can be removed easily. ALD is also a promising method in the production of solar cell absorber and optical coatings.

2.1.4 Comparison to Other Thin Film Process Techniques

Thin film deposition technologies can be divided into three major generic categories: (i) physical vapor deposition (PVD), (ii) gas-phase chemical deposition methods, and (iii) liquid phase chemical film formation techniques.[42] PVD includes the evaporative methods and glow-discharge technologies. In the evaporative methods, a vapor of a source material is generated and transported to the substrate to condense on the surface of it. The requirements to the working condition and substrate motion are strict. Glow-discharge technologies include sputtering and plasma deposition. Similar to evaporative methods, the vapor of electrode material is generated with the help of bombarding ions during the process, and then the vapor is transferred from the sputtering target to the substrate in vacuum. Gas-phase chemical deposition methods require materials formed by chemical reaction between vapor phase constituents in the gas phase on the surface of substrate. Liquid phase chemical formation is accomplished mainly by electrochemical process or chemical deposition process. The media used in the techniques is generally liquid.[42]

A benefit of ALD is that the self-limitation of the surface reaction generates exactly the same amount of materials on the substrate, thus the thickness of deposited films can be easily and precisely controlled by the number of reaction cycles.[9] By comparison, other deposition methods cannot control the growth of film in atomic layer and they can only estimate the thickness of the coating in a certain time. During the ALD process, the precursor flux doesn't need to be uniform to the substrate attributing to the self-limiting growth mechanism. But the flux needs to be large enough to saturate the substrate surface. This enables the ALD to

fabricate large-area and large-batch samples that are only limited by the size of reaction chamber.[9] In the physical vapor deposition methods, the substrates are required to be placed in a certain position to get uniform coating.

The ALD coating is very smooth and conformal to the substrate even on high aspect ratio structures because the gas phase precursors can fill all spaces due to long mean free path under vacuum condition (5×10^{-3} cm at 1 Torr), and reactions in each cycle are driven to completion.[5] The films are also continuous and pin-hole free because no surface site is left behind during the reaction. The excess precursors are purged out of the reactor before the co-reactants are delivered to the reactor. In comparison, CVD growth results in the formation of granular surface caused by the gas phase materials nucleation, and a poor uniformity are observed. The uniformity of evaporative films is also very poor. Although the films obtained through sputtering are uniform to the substrate, the grain size on the films is large. In the physical vapor deposition methods, the reactor may be evaporated or sputtered during the process and leads to metal and particle contamination of deposited films. This phenomenon won't happen in chemical vapor deposition methods

One major limitation of ALD is the general slow deposition rate of the vapor cycling since only one atomic layer can be obtained after one cycle. The typical deposition rate of ALD is 100-300nm/h.[9] In comparison, E-beam evaporation has a deposition rate of 10-100 Å/s. The deposition rate of sputtering is ~100 Å/s for metal materials and 1-10 Å/s for dielectric materials. CVD has a deposition rate of 10-100 Å/s. However, low deposition rate doesn't necessarily mean low productivity per time unit. The large area processing capability of ALD

compensate for its low growth rate. Another limitation of ALD is the lack of good precursors or processes for some important materials.

2.2 ALD on Polymers

ALD process can deposit smooth, conformal, defect free inorganic layers on a wide range of material types. The low temperature materials growth in particular has allowed for an investigation to polymer substrates. Prior research in this field is reviewed in the following sections.

2.2.1 Growth Mechanisms of ALD Coatings on Polymers

Materials growth by ALD on organics has shown that various end-group terminations on organic materials will greatly affect the nucleation and growth behaviors.[43, 44] Xu et al.[43] investigated the surface reactions between precursor TMA and self-assembled monolayers (SAMs) terminated with different functional groups during Al_2O_3 ALD. They show that aluminum oxide easily nucleates and grows on $-\text{OH}$ terminated SAMs because of high thermodynamic driving force, while for $-\text{NH}_2$ or methyl group terminated SAMs, the precursors diffused into the monolayer.[43] Same phenomenon has been observed for polymer containing different functional groups, such as polyvinyl alcohol (PVC), polyamide-6 (PA-6) and polypropylene (PP).[45] For example, FTIR results indicate enhanced reactivity between TMA and PVA's hydroxyl groups, and between TMA and PA-6's amide bond unit, resulting in insertion of methyl groups, during the initial cycle of reaction. In comparison, no chemical interaction between TMA and PP, an inert polymer with no functional groups, was observed under FTIR and quartz crystal microbalance (QCM) measurement.[45]

An initial model by Wilson et al. [44] was proposed in 2005 that outlines the ALD nucleation and growth on polymers through their investigation of aluminum oxide growth on PS, PE, PVC, PP and PMMA using QCM. Their research results show that during the first several cycles of ALD, the mass gain on polymers varies significantly for different polymers. These effects are resulted from the diffusion and retention of precursors into the polymer. Specifically, diffusion is related to the porosity on the surface of films and the retention of precursors is associated with the chemical solubility of precursors in polymers. Hence is concluded that Al_2O_3 ALD on polymers with no reactive groups, such as PP, involves the following steps: reactant diffusion into the near surface region of the polymer film, Al_2O_3 cluster formation, and Al_2O_3 cluster coalescence to fill the space between polymer chains, forming a continuous inorganic film on polymer, as shown in figure 2.2.[44]

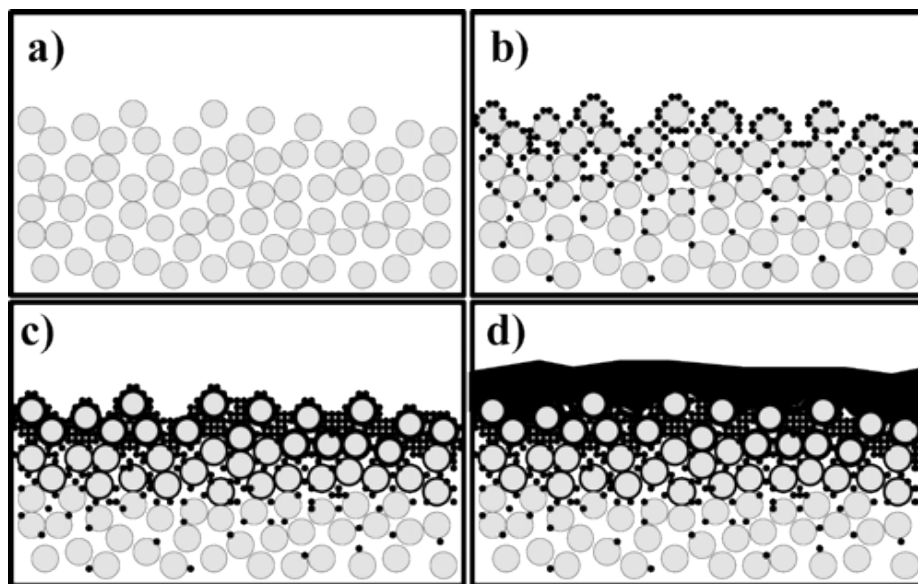


Figure 2.2. Growth model for Al₂O₃ ALD on polymers with (a) cross section of polymer films in which the polymer molecules are shown by circles and loosely packed; (b) reactant diffusion into the polymers; (c) aluminum oxide cluster to fill the space between polymer chains and (d) formation of continuous Al₂O₃ film. From Wilson et al..[44]

A limitation to this model is that it is only fit for the polymers with no functional groups. Additional work has begun to create a model for the complex process of ‘infiltration’ which means the precursor can diffuse into the polymer and react with the polymer backbone at the same time.

The temperature effect on nucleation and growth of aluminum oxide on nonreactive polymer, such as polypropylene, has also been studied.[12] Transmission electron microscope images of polypropylene with ALD alumina coatings at different temperatures demonstrate that higher process temperature leads to enhanced subsurface growth, which is ascribed to

polymer expansion at high temperature and further penetration of precursor into the polymer bulk region,[12] which is in agreement with the model proposed by Wilson et al..[44]

Interestingly, plasma-enhanced ALD generally has exhibited little subsurface nucleation into the polymer matrix because the oxygen plasma can add functional groups, such as –OH, to the surface of the polymer during the early stage of the reaction.[41] The precursors will react with those hydroxyl groups and form a continuous film on the surface of the polymer.

2.2.2 Barrier Properties of ALD Coatings on Polymers

A key potential application of ALD to polymers is that of a diffusion barrier on flexible organic devices such as organic light emitting diode (OLED) and organic thin-film transistors (TFTs). Due to high water vapor permeation rate of polymeric materials, the water and oxygen molecules can easily penetrate the substrate to cause delamination and oxidation of metal cathode, therefore limiting lifetime of these organic electronics and restricting the commercialization of them.[46] Generally, a device with 10000 hr lifetime requires a water vapor transmission rate (WVTR) of $<5 \times 10^{-6}$ g/m²/day while most polymeric materials have a WVTR of $\sim 10^1$ - 10^{-1} g/m²/day.[46, 47] To improve the water barrier property of polymers, a pinhole free, continuous coating of inorganic material on the polymer is an ideal.

Nanoscale inorganic layer deposited by ALD have shown excellent WVTR barrier properties. Groner et al.[48] have previously shown the oxygen transmission rate and WVTR of ALD films of different thickness on PEN. The 26 nm single-sided Al₂O₃ ALD on PEN has an oxygen transmission rate lower than the test limit of MOCON instrument and a WVTR lower than 10^{-3} g/m²/day. Carcia et al.[23] later reported that 25nm Al₂O₃ ALD coating deposited

on PEN at 120°C has a permeation rate of 1.7×10^{-5} g/m²/day at 38°C and 6.5×10^{-5} g/m²/day at 60°C using a Ca test. The moisture transmission rate is estimated to be less than 10^{-5} g/m²/day at 23°C. For comparison, the 20nm thick PEALD alumina deposited at room temperature on PEN has shown a WVTR of 5×10^{-3} g/m²/day.[41]

To further enhance the water vapor barrier properties of the coating, multilayer coatings consisting of inorganic films and/or organic films deposited by ALD processed have been explained.[2, 24, 25] For example, an Al₂O₃/SiO₂ bi-layer shows a decrease in WVTR from 1×10^{-3} g/m²/day to 1×10^{-4} g/m²/day. For a Al₂O₃ only layer, SiO₂ has shown to efficiently fill the pinhole defects in single alumina layer, the main factor causing water permeation into the polymer.[24] The deposition of 5nm thick ALD alumina on 100nm SiN PECVD films also reduced the WVTR to less than 5×10^{-5} g/m²/day at 38°C/85% RH owing to either sealing of grain boundaries of SiN or improved nucleation of Al₂O₃ on SiN.[25] While the multilayer inorganic materials have shown a decrease in WVTR, the brittleness of the ALD films have led to cracking initiated by handling and mounting. One proposed solution to this issue is to insert a soft polymer layer between the inorganic layers, forming alternating inorganic and organic layer pairs.

Polymer/inorganic multilayer stacks have different degradation mechanisms from multilayer inorganic materials. As the polymer layer is flexible, it will not be cracked under bending force. The moisture diffused through the cracks on inorganic coatings needs to go through the polymer to reach the cracks on another inorganic coating. This results in a path length that is much longer than the polymer physical thickness, preventing the diffusion of moisture

into the encapsulated device in an effective way. Various polymer/inorganic multilayer system have been studied.

Vitex System, Inc reported flexible encapsulation layers composed of alternating alumina and polyacrylate layers. The alumina layer can be sputtered via plasma or deposited using ALD. The Organic layers are deposited by evaporation of the monomer followed by curing.[2] When the thickness of sputtered inorganic layers is tens of nanometers and polymers are in micrometer range, the lifetime of the device is about 2500h which is a quarter of the performance of glass encapsulated device.[2] Park et al also explained the structure of multilayers of Al_2O_3 /Aluminum Alkoxide (Alucone) deposited on polymer by ALD and molecular layer deposition (MLD) process.[2] Alucone is a kind of hybrid organic-inorganic polymer-like film. No specific WVTR is given to this structure.

2.2.3 Other Applications of ALD Coatings on Polymers

Other than as water diffusion barrier, ALD inorganic coatings have also exhibited the ability to change the surface properties of different polymers and fibers.[20, 22, 49, 50] Ten titanium nitride ALD cycles on cotton fibers shows a much larger contact angle of 116° compared with 0° of uncoated cotton fibers, attributing to an increase in fiber rigidity by the inorganic coatings that greatly reduce the contact area between fiber and droplet. As the TiN coating is also biocompatible, it has also shown to enhance cell growth and adhesion on the surface of fibers.[50] The function of alumina on cellulose fibers is also investigated, where an abrupt transitions from naturally hydrophilic state to a metastable hydrophobic state is observed with a thin alumina coating (one TMA/water cycle). After ten cycles ALD, the cellulose

fiber will become wetting again.[22] This phenomenon can be inferred that the thin alumina coating reacted with the fiber surface promoting the surface roughness while thick alumina smoothen the surface efficiently. For naturally hydrophobic surface such as polypropylene, the alumina ALD deposition produces a hydrophilic surface when the deposition temperature is low. At high deposition temperature, the polypropylene fibers remain hydrophobic after ALD processing.[22] This is because high temperature enhances diffusion of precursors into polymers, resulting in island nucleation which results in a hydrophobic surface, while low deposition temperature results in a conformal thin film on surface of the fiber.

The alumina coating altered the surface of PDMS from hydrophobic to hydrophilic, but a quick recovery to hydrophobicity is found on PDMS when the sample is exposed to ambient condition for over 48 hours, ascribed to the out-diffusion of small molecules through cracks of ALD coating.[49] Kemell et al.[20] studied the wettability of alumina and titanium oxide on different polymers including PEEK, PMMA, PTFE and ETFE, and found that Al_2O_3 and TiO_2 coatings decrease the water contact angle on all polymers. The effect of TiO_2 coating becomes much more obvious upon UV illumination, enabling wettability modification of hydrophobic fluoropolymers.

ALD can also be applied to polymer films and fibers for the fabrication of nanostructures. ALD has been used as a method to produce microtubes with smooth surface and precisely controlled wall thickness by applying ALD on polymer microfibers and then removing the polymer core during calcination or sonication.[51] Peng et al. obtained uniform alumina microtubes after heating Al_2O_3 -coated electro spun poly(vinyl alcohol) nanofibers in air at

400 °C for 24 hours. The thickness of the wall can be adjusted by choosing different number of ALD cycles.

ALD technique can be used to fabricate ultralight X-ray mirrors with adjustable curvatures by depositing multilayer of W/Al₂O₃ on flexible polyimide and PEN polymers.[52] Between the polymer and 6-bilayer W/Al₂O₃ nanolaminates films, 100 cycles alumina ALD was performed to smooth the surface of the polymer to obtain high X-ray reflectivity. The growth of tungsten and alumina bi-layers also produce ultrasmooth interface because the self-terminating reaction of ALD effectively prevents roughness during the process. The precise thickness control to the bi-layers is another way to enhance the X-ray reflectivity which is measured to be 78% and 74% on polyimide and PEN, respectively, closing to 80% on silicon wafer.[52] In addition, the free standing W/Al₂O₃ superlattice is obtained after removal of polymer substrate.

2.2.4 Comparison to Other Techniques for Inorganic Coatings on Polymers

Deposition of inorganic coating on polymers has become more and more important in the development of many devices including electronics, mechanical and biomedical applications.[53] The deposition methods of inorganic films usually include sputtering, CVD, ALD, sol-gel and thermal-spray. However, sputtering and thermal-spray methods require high level of energy to perform the deposition and the high energy may damage the polymer surface because of high heat sensitivity of some polymers. A primary advantage of ALD is its low deposition temperature compared with other techniques, making it an ideal method to deposit inorganic films on heat-sensitive polymers. The uniformity and conformality of ALD

films and the thickness control to it are also better than the films deposited using other techniques.

The significant difference in surface energy between inorganics and polymers has led to poor interfacial strength. In many materials processes, this led to delamination.[53] An advantage of ALD is the enhanced adhesion between the inorganic films and the polymer surface, as a result of surface reaction nucleation. For polymers with large amount of reactive sites on the surface, the inorganic films deposited by ALD can form covalent bonds with substrate, increasing the interfacial strength. This adhesion may be enhanced much more for polymers which allow for precursors to diffuse into the polymer subsurface and form a hybrid layer at the interface of the coating and polymer. Often in other deposition methods, the lack of a covalent bond between the coating and substrate results in a poor quality.

WVTR barrier properties of the inorganic films on polymers have been shown to vary significantly based on the deposition techniques employed. A single layer sputtered Al_2O_3 (~80nm thick) could improve the moisture barrier of poly(carbonate) (PC) by two orders of magnitude, poly(ethylene terephthalate) (PET) by one order but no improvement to poly(ethylene naphthalate) (PEN).[54] By comparison, the barrier properties of ALD films are much better, as shown in Part 2.2.2. Moreover, the sputtered coating requires the substrate surface to be very smooth and cannot be applied on the polymer with high aspect ratio.

2.3 Mechanical Properties of ALD Coatings

Despite the increased understanding of ALD on a wide range of materials, processing on different materials needs clarify. Few studies have explored the mechanical performance of ALD films. Mechanical properties of ALD coatings play a key role in the process integration compatibility and long-term reliability of devices. This is especially true for applications on flexible substrates, where fracture of ALD coatings may occurs during the handling or processing. This section reviews 1) the fracture mechanisms of thin films, 2) the mechanical properties related to fracture mechanisms and the test methods to these properties, 3) ALD thin film behavior and 4) comparison to other films deposited using different techniques.

2.3.1 Fracture Mechanisms of Thin Films

Fracture is referred to as the total or partial separation of a body or structure, generally caused by propagation of one or several cracks on the material. Thus the fracture mechanics mainly deals with the study of crack propagation in materials.[55] For hard films on soft substrates, the fracture of films under tension will be prevented by the substrate and channeling forms in the coating layer. The fracture mechanics can be divided into linear elastic fracture mechanics, also referred to as brittle fracture mechanics, and nonlinear fracture mechanics.[55] As the fracture behavior of thin alumina film is dominated by elastic fracture, only the linear elastic fracture mechanics is introduced in this section.

Crack formation occurs when the tension in the film exceeds the film's tensile strength σ_c . The lateral propagation of cracks is related to the stress intensity factor, K_I . In two-dimensional problem of a body which contains a straight crack, the small region around the

crack end with radius, R , is defined as crack tip field. This is shown in Figure 2.3.[55] When the crack is loaded by a pair of opposing forces at the crack faces, stresses will concentrate around the crack tip field. This value, K_I , is used to characterize the stress of crack tip field. For bulk material, K_I is related to the crack length, L . But for thin films on a surface, K_I depends only on the thickness of the film, t , and not on the crack length,[56] following:

$$K_I = \kappa_I \left(\frac{E_f}{E_s}, \frac{\sigma}{Y} \right) \sigma \sqrt{t}$$

where κ_I is the geometry factor and generally depends on the elastic properties of the film and substrate, E_f and E_s are the elastic modulus of the film and substrate, and Y is the uniaxial yield strength of the substrate. Once the stress intensity factor induced by the tensile stress exceeds the fracture toughness of the film, lateral crack propagation occurs in the film.

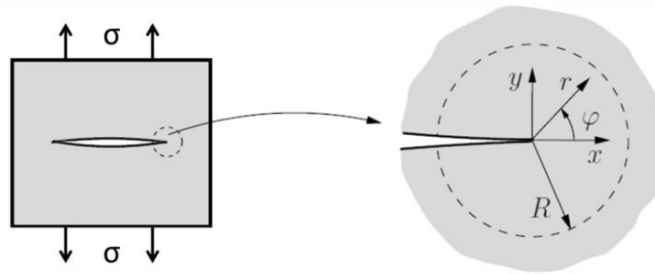


Figure 2.3. Schematic of crack tip field.[55]

An additional mechanism to explain the crack propagation is called energy criterion. This model was first proposed by Griffith who suggests that crack propagation follows an energy balance:[55]

$$d\Pi^{int} + d\Pi^{ext} + d\Gamma = 0$$

Here, Π^{int} is the internal strain energy, Π^{ext} is the external force energy, and Γ is the fracture energy which is an evaluation of the surface energy change by formation of two new fractured surfaces. Due to the crack growth by a length, Δa , the system passes from an equilibrium state I to another equilibrium state II. During this process, internal mechanical energy will be released. According to this model, during crack initiation and subsequent crack propagation, the released energy must be equal to the energy needed for fracture.[55] By computing the potential energy stored in a specimen and free energy change as a function of crack length, the following relationship is determined:[57]

$$\sigma\sqrt{a} = \sqrt{\frac{EG}{\pi}}$$

where a is the length of crack, E is the young's modulus of materials, and G is strain energy release rate, defined as the change in elastic strain energy per unit area of crack growth. This equation only fits for the bulk material. For a film on substrate system, no specific definition is given. However, it is apparent that the plastic part of the system will dissipate some energy. The dissipation effect is influenced by kinds of substrate and connection between the substrate and the film.

In general, the two mechanisms outlined deal with the propagation of an isolated crack. The growth of multiple cracking in the films can be explained by the shear lag model.[58] When the cracks are induced in the films, the films are divided into many segments (Figure 2.4). For one segment with width L , the load applied on the specimen is not transferred directly to it. At the two ends of this segment, the interfacial shear stress has the maximum value, while

the interfacial shear stress is zero at the center of segment. The load transfer length is λ . The tensile stress in the films takes the maximum value at the center of segment. When the applied load is increased until σ_f exceeds some critical value, a new crack will form at the center and the distance between two cracks becomes $L/2$. Once L is smaller than λ , the shear stress areas at the two ends of segment overlap each other, resulting in partial cancellation of shear stress and the decrease in σ_f , leading to saturation of crack density.

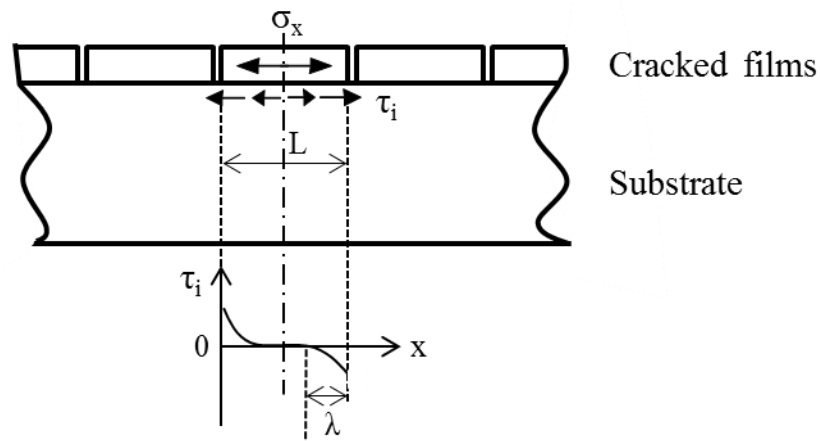


Figure 2.4. A two dimensional model of stress distributions in a cracked film. σ_x , τ_i and λ are tensile stress in the film, interfacial shear stress, and load transfer length, respectively.

2.3.2 Mechanical Properties and Their Test Methods

The fracture mechanics proposed by Griffith also lead to the concept of fracture toughness. The fracture toughness describes the ability of a material to resist fracture after a crack is initiated, and is denoted by K_{IC} , which has the units of $\text{Pa}\cdot\text{m}^{1/2}$. This value provides a quantitative way of expressing a material's resistance to brittle fracture after the point at

which a crack forms.[59] If a material's fracture toughness is very high, it is likely undergo a ductile fracture. Brittle materials generally have relatively low fracture toughness.

For thin films on a thick substrate, Beuth has constructed a model to predict the fracture toughness of thin films when a crack is perpendicular to the film/substrate surface with crack tip touching the interface.[60] The model provides an expression of steady-state energy release rate, G , following:

$$G = \frac{\pi t_f E_f \varepsilon_a^2}{2(1 - \nu_f^2)} g(\alpha_D, \beta_D)$$

where the coefficient $g(\alpha_D, \beta_D)$ represents the elastic misfit between the substrate and the films, and α_D and β_D are the Dunder's parameters (unitless).[60] The energy release rate required to form cracks in the film is given as:

$$\Gamma = \frac{K_{IC}^2}{E_f}$$

where Γ is the critical energy release rate, meaning if the energy release rate reaches the critical value, Γ , the isolated cracks will be initiated. At this circumstance, the applied strain ε_a equals to the critical tensile strain ε_c . Hence, the critical tensile strain is defined as the strain at which the film starts to crack.

The tensile test or bending test can be used to determine the critical strain of the film. While the tensile test is easier to perform, a bending test is more often used to better simulate the fracture of films in handling.[61] Figure 2.5 shows the schematic illustration of the sample configuration and test setup.

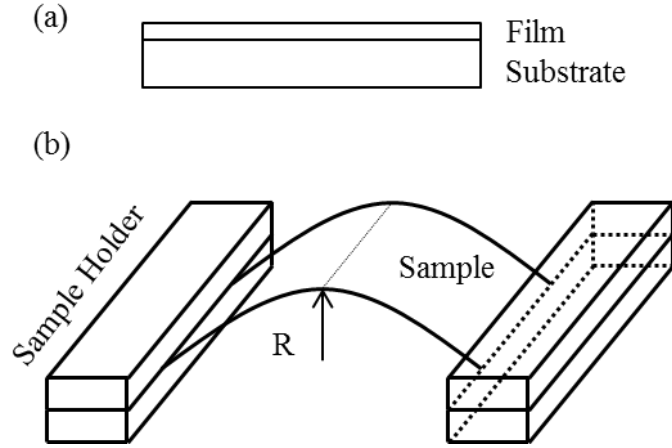


Figure 2.5. Schematic diagram of **(a)** sample configuration and **(b)** holders and bent films on flexible test apparatus.

The sample in the length of L is held between the two parallel holders and bent into a cylindrical curve by moving one holder with respect to the other. The displacement of the holder is recorded as ΔL . It is noticed that the test method is more like a buckling case, so the condition of uniform curvature is not true. By assuming the bent shape of the sample to be a sinusoidal curve, the radius of curvature r at the center can be expressed as [61]:

$$r = \frac{L}{2\pi \sqrt{(\Delta L/L) - (\pi^2(t_f + t_s)^2/12L^2)}}$$

where t_f and t_s are the thickness of the film and the substrate, respectively. Due to the mismatch between the elastic modulus of the film and substrate, the neutral surface of the sample is shifted. Then the film strain expression should be modified and given as:

$$\varepsilon_a = \left(\frac{t_f + t_s}{2r}\right) \frac{(1 + 2\eta + \chi\eta^2)}{(1 + \eta)(1 + \chi\eta^2)}$$

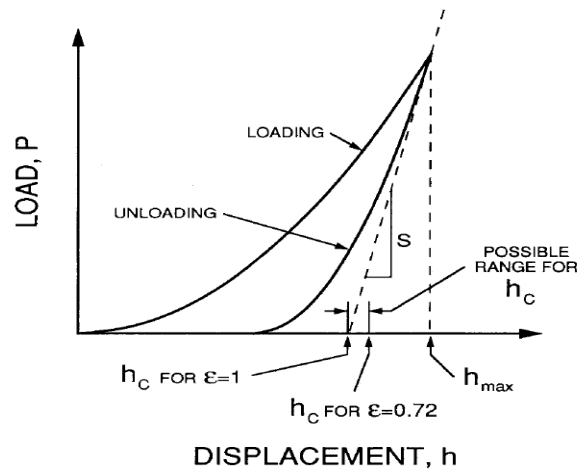
where $\eta = t_f/t_s$ and $\chi = E_f/E_s$. After recording the ΔL at which the first crack appears, it is easy to calculate the critical tensile strain in the bending test using the above two equations.

Fracture toughness is also closely related to the elastic modulus of material. For thin films on a thick substrate, nanoindentation can be applied to the film's property. Nanoindentation is a simple method to measure the elastic modulus and hardness of one material through penetrating the material using a tip with known properties at either a constant loading rate or a constant displacement rate.[62] During the nanoindentation process, the instrument records the load applied on the tip and its displacement, and obtains a typical load-displacement curve, as shown in Figure 2.6a. Then the following equations are used to calculate the contact modulus and the hardness of the sample.[16]

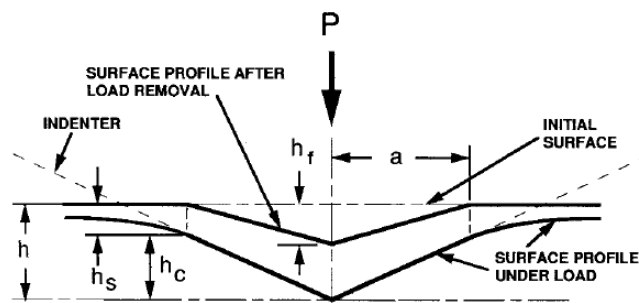
$$S = \frac{dP}{dh} = \frac{2}{\sqrt{\pi}} E_r \sqrt{A}$$

$$H = \frac{P_{\max}}{A}$$

Here, S is the measured stiffness calculated from the upper portion of the unloading curve, E_r is the combined elastic modulus of sample and indenter, A is the contact area, H is hardness of specimen and P_{\max} is the peak indentation load.



(a)



(b)

Figure 2.6. (a) A representative load versus indenter displacement curve showing quantities used in an analysis and (b) a representative cross section through an indentation with different quantities.[16]

With the development of sub-micron indentations, direct observation method to obtain the contact area became difficult as the small indentation was difficult to image. New methods based on the indenter shape and indentation load-displacement curve was required. The most widely accepted method to determine the contact area was given by Oliver and Pharr,[16]

who considered the non-elastic contact, believing the contact area between the indenter and specimen changed continuously and the unloading portion of the load-displacement curve is non-linear. The expression of contact area is described as

$$A = C_0 h_c^2 + C_1 h_c + C_2 h_c^{1/2} + C_3 h_c^{1/4} + \dots + C_8 h_c^{1/128}$$

where $C_0, C_1 \dots C_8$ are constants. h_c is the contact depth. From the Fig. 2.6, it is noted that,

$$h_c = h_{\max} - h_s$$

From Sneddon's expressions that apply for a conical indenter and elastic component of the displacement, Oliver and Pharr derived an equation for h_s :

$$h_s = \epsilon \frac{P_{\max}}{S}$$

where ϵ is the geometry of indenters, being 0.75 for Berkovich indenters.[62]

To find the area function, Oliver and Pharr used the large indentations on aluminum due to its low hardness. The area function for a perfect Berkovich tip was found to follow the expression:[16]

$$A(h_c) = 24.5 h_c^2$$

Combining the above several equations, we can obtain the combined elastic modulus, E_r .

Then the elastic modulus of the sample is obtained using,

$$\frac{1}{E_r} = \frac{1 - \nu_i^2}{E_i} + \frac{1 - \nu_s^2}{E_s}$$

where the E_i and ν_i are Young's modulus and Poisson's ratio of indenter, and E_s and ν_s are the parameters of specimen.[62]

It is important to note that when performing nanoindentation on a coating/substrate system, the coating thickness should be more than ten times the indentation depth. This ensures that the property of the coating is not affected by the substrate. ISO 14577 defines another method to get the properties of the coating.[63] According to the standard, the contact modulus and hardness of thin coating on substrate can be determined by extrapolating to zero contact depth on the plot of contact modulus vs. contact depth. To assess the contact modulus of the hard coatings on soft substrate, the extrapolating is taken in the range $a/t < 2$ where a is the radius of the contact area and t is the total thickness of the coating. For an ideally sharp Berkovich tip, $a = 2.79h_c$ and the criteria can be given as $h_c/t < 0.7$.

2.3.3. Fracture Behavior of ALD Coatings

Studies have investigated the critical tensile strain and saturation cracking density of alumina ALD coatings grown under different conditions by applying tensile force on those samples.[64-67] Figure 2.7 compares the critical tensile strain of ALD alumina coatings of varying thicknesses on polymer substrates. The critical tensile strain and the saturation crack density is found to scale as $(1/h)^{1/2}$, where h is the coating thickness.[64]

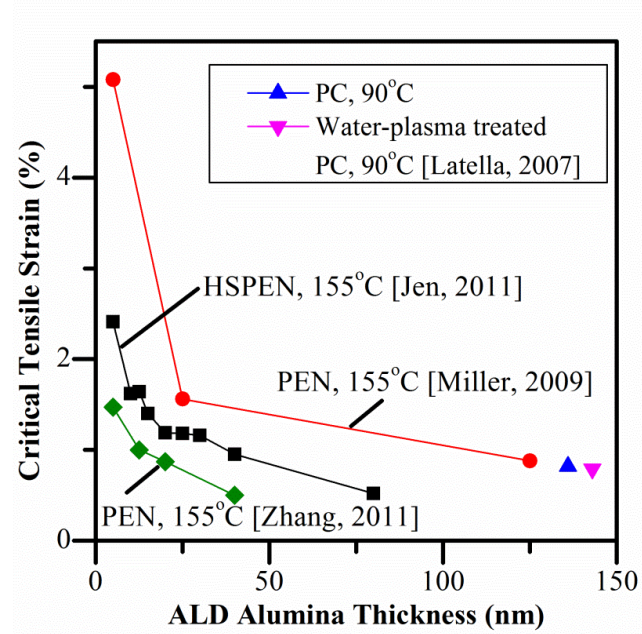


Figure 2.7. Critical tensile strain of different thick Al_2O_3 ALD coatings on different polymers. The temperature represents the deposition temperature of ALD process.

As Fig.2.7 shows, the critical tensile strain of ALD alumina coating varies significantly among the available research data. Jen,[64] Miller,[65] Zhang[66] and Latella[67] all deposited the alumina at the same thickness on PEN at 155 °C, obtaining a different critical strains. The difference is attributed to the variable surface treatment of the PEN substrate, as well as the varying sensitivity of the optical probing. Typically, high sensitivity of optical probing allows for the crack formation to be visualized better at low tensile strain. In the studies, the fracture toughness of alumina thin films were found to be $1.89 \pm 0.1 \text{ Mpa}\cdot\text{m}^{1/2}$ by Miller, $2.3 \pm 0.24 \text{ Mpa}\cdot\text{m}^{1/2}$ by Jen and $0.23 \text{ Mpa}\cdot\text{m}^{1/2}$ by Latella et al.[67] In comparison to bulk alumina with a fracture toughness of 3-5 $\text{Mpa}\cdot\text{m}^{1/2}$ [59], the low value may be due to the high porosity as a result of low deposition temperature and high film thickness.

The elastic modulus of different ALD alumina coatings reported by the use of nanoindentation is listed in Table I. Although different indentation depth is used in different studies, all results were corrected to reduce the effect of the substrate.

Table 1. Elastic modulus and Berkovich hardness of ALD Al₂O₃ coatings

Substrate	Deposition Temperature (°C)	Coating Thickness (nm)	Elastic Modulus (Gpa)	Hardness (Gpa)	Reference
Silicon	80	150	125 ± 6	4.83 ± 0.09	[18]
Silicon	150	160	172 ± 9	6.44 ± 0.12	[18]
Silicon	155	500	195.3 ± 20.1	6.65 ± 0.80	[15]
Silicon	177	300	180 ± 8.2	12.3 ± 1.0	[13]
Silicon	300	60	220 ± 40	10.5 ± 1.0	[14]
PET	80	~180	36.2 ± 1.8	2.05 ± 0.09	[18]
PET	150	~160	43.7 ± 0.7	2.46 ± 0.08	[18]

This table shows the elastic modulus and hardness of ALD alumina coatings on silicon and PET substrate. The ALD coatings were deposited under different temperatures. With the increase of deposition temperature, both the elastic modulus and hardness of alumina coating show an increasing trend. The alumina coating on silicon has a higher modulus and hardness than that on the PET substrate, attributing to the soft substrate effect.

2.3.4 Comparison to Other Deposition Techniques

Most often, thin films produced by ALD are characterized as amorphous. These films have different uniformity and structures from the films grown through other techniques. Hence, the mechanical properties of films are dependent on the deposition technique. Table 2 compares literature data on the mechanical properties of thin films produced by different technique.

Table 2. Mechanical properties of various materials

Materials	Thickness (nm)	Fracture Toughness K_{IC} (Mpa·m ^{1/2})	Elastic Modulus E (Gpa)	Hardness (GPa)	Reference
ALD Al ₂ O ₃	--	1.89 ± 0.1	195.3 ± 20.1	6.65 ± 0.80	[15, 65]
Sputtered Al ₂ O ₃	16000	2.1 ± 0.3	158	7.3	[68]
Al ₂ O ₃ annealed at 1600°C	--	4.2-4.3	--	17-18	[69]
Al ₂ O ₃ ceramic	--	3-5	375	1.44	[70]
ALD HfO ₂	60	--	220 ± 40	9.5 ± 1.0	[14]
Sputtered HfO ₂	159 ± 4	--	166 ± 8	8.4 ± 0.4	[71]

The table shows that the mechanical properties of amorphous alumina films grown from ALD and sputtering are similar, but much lower than that of crystallized alumina obtained after annealing. The low hardness of alumina ceramics is due to the different measurement methods. The atomic layer deposited HfO₂ has higher elastic modulus and hardness than the sputtered films.

In this study, effects that the growth behavior of ALD alumina on PA-6 and a printed circuit board have on the mechanical properties of these polymers are examined. The formation of hybrid layer between the polymers and ALD coatings are shown to influence the mechanical properties of the ALD coating. The mechanical properties of ALD coatings on polymers are examined through standardized nanoindentation and bending tests

3. EXPERIMENTAL

3.1 Material Preparation

In this study, spin cast polyamide-6 (PA-6) films, freestanding PA-6 films and PSR-4000 sheet directly cut from printed circuit board were used. PA-6 solution for spin casting was prepared by dissolving PA-6 granules into formic acid. PA-6 granules (Ultramid® B27E 01) were purchased from BASF and used as received without further purification. Formic acid (~98% purity, CAS No. 64-18-6) was obtained from Sigma-Aldrich®. 2 droplets of the solution were dispensed onto a silicon substrate. The size of the solution was about $\frac{1}{4}$ of the Si substrate size. The solution was spun cast at different speed for 60 seconds, and then annealed at 90 °C for 60 seconds. The resulting film thickness was determined by ellipsometry (J. A. Woollam Co., Inc.) with Cauchy model. Fig.3.1 shows the film thickness under different spinning speed obtained from two PA-6 solutions.

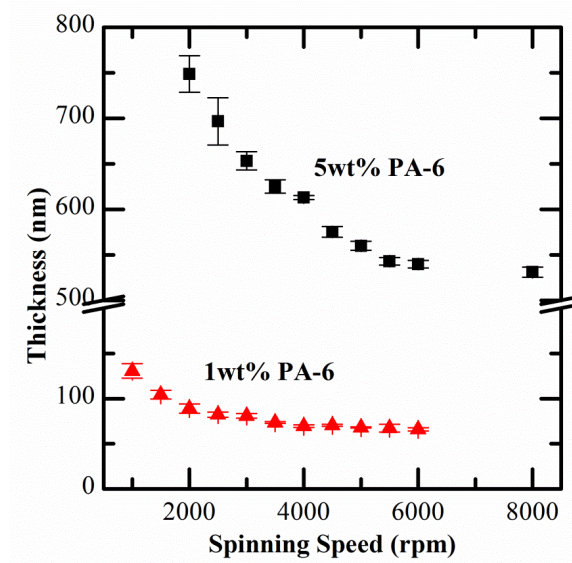


Figure 3.1. Thickness of spin cast PA-6 films as a function of spinning speed.

Figure 3.1 indicates that PA-6 solution with high concentration leads to thick films. With the increase in spinning speed, the spun cast films become thinner and variation in the film thickness become smaller. As thick films were needed in the nanoindentation test, the 5 wt% PA-6 solution was used. 3000 rpm was chosen as the spinning speed to make sure the film surface is smooth. The 5 wt% PA-6 solution was obtained by dissolving 1.28 g PA-6 into 20 mL formic acid and then stirring for about 2 hours.

For the crack evaluation in the bending testing, 0.1 mm thick freestanding PA-6 films were purchased from GoodFellow® Inc. The films are transparent, which makes the cracks in ALD coatings visible. The density of purchased films is 1.13g/cm³.

PSR-4000 is a commercial polymer typically used in the fabrication of flexible printed circuit boards. The composition information is not available through the company, but FTIR shows carbonyl and carbonate groups in it, suggesting it is most likely an acrylic based polymer. As a printed circuit board material, it is used due to its wide processing window, low odor, excellent solder ball resistance, compatibility with lead-free processing and hard surface finish. PSR-4000 sheets used in this study were cut directly from the margin of printed circuit boards obtained from Sandia National Lab. It can also be produced through screen printing the combination of PSR-4000MP and CA-40MP.

3.2 ALD Processing

3.2.1 ALD Reactor

Aluminum oxide ALD growth was performed in a custom hot wall, flow tube reactor system (Figure 3.2). The reactor body consists of a conflate tube, ~90 cm in length and ~20 cm in

diameter, evacuated with a mechanical pump to a base pressure of ~ 0.03 Torr. The pressure of the reactor is controlled by a mass flow controller through adjusting the flow rate of carrier gas (nitrogen). The temperature of the reactor chamber is controlled by resistive heat tapes through a temperature controller (OMEGA®, Model CN 616). The reactor operates with an inert carrier gas in viscous flow.[5] Prior to entering the system, the nitrogen is flowed through a Areonex Gatekeeper Ni-catalyst filter which reduces the water content to less than 1 part per trillion. Diethylzinc(DEZ)/water and trimethylaluminum(TMA)/water are precursors of ZnO and Al₂O₃. They are introduced into the chamber through the entrainment of nitrogen.

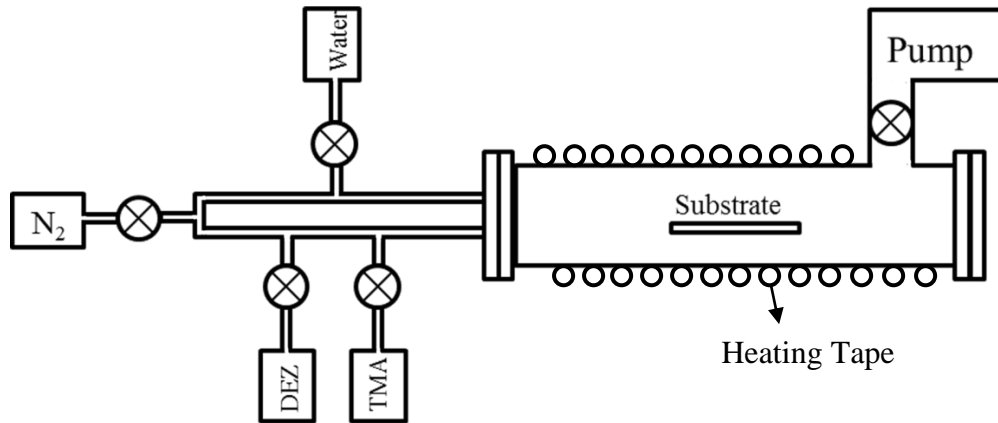


Figure 3.2. Schematic diagram of the ALD reactor used in this study.

3.2.2 ALD Processing of Alumina

During the ALD processing, a pressure of 1 Torr ultrahigh purity N₂ (99.999%, National Welders) was maintained using a mass flow controller. Alumina was deposited on spun cast thin films, free standing films, PSR-4000 sheets and bare silicon wafers by alternating

exposures of trimethylaluminum (TMA, 98% purity, STREM chemical) and water (Sigma Aldrich, CAS No. 7732-18-5). The same ultra-high purity nitrogen was used as a carrier gas. It was also used to purge the chamber between exposures of reactants. Typical ALD cycle times were $\text{TMA}/\text{N}_2/\text{H}_2\text{O}/\text{N}_2 = 0.2/30/0.2/45\text{s}$.

The temperature window of ALD growth in the processing system was evaluated. The ALD temperature window describes the ideal processing temperature range in which the growth is saturated. Figure 3.3 shows the ALD window between the nonideal regions. When the temperature is too low, the precursor may condense onto the substrate, leading to higher growth rate. It is also possible that the reaction is incomplete due to the low kinetics and low growth rate is observed. If the temperature is too high, the precursors, like water, may re-evaporate, resulting in lower growth rate. The decomposition of precursors may also happens which increases the growth rate.

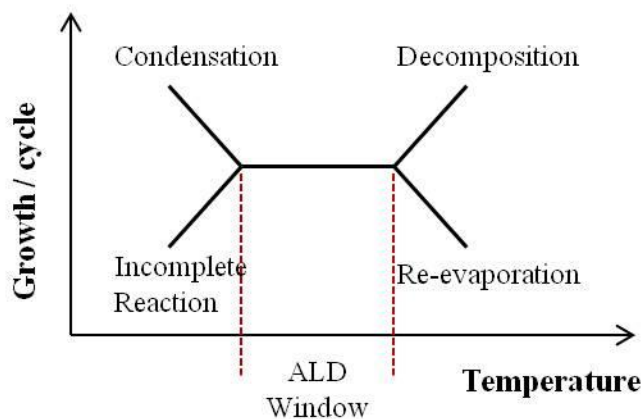


Figure 3.3. ALD growth per cycle at different temperatures.

The growth rate of ALD alumina was examined in the range of 40 °C to 150 °C by dividing the thickness of 50 cycles ALD coatings with the number of cycles. The thickness of alumina coating was measured using spectroscopic ellipsometry. Figure 3.4 shows the growth rate of aluminum oxide films as a function of deposition temperature.

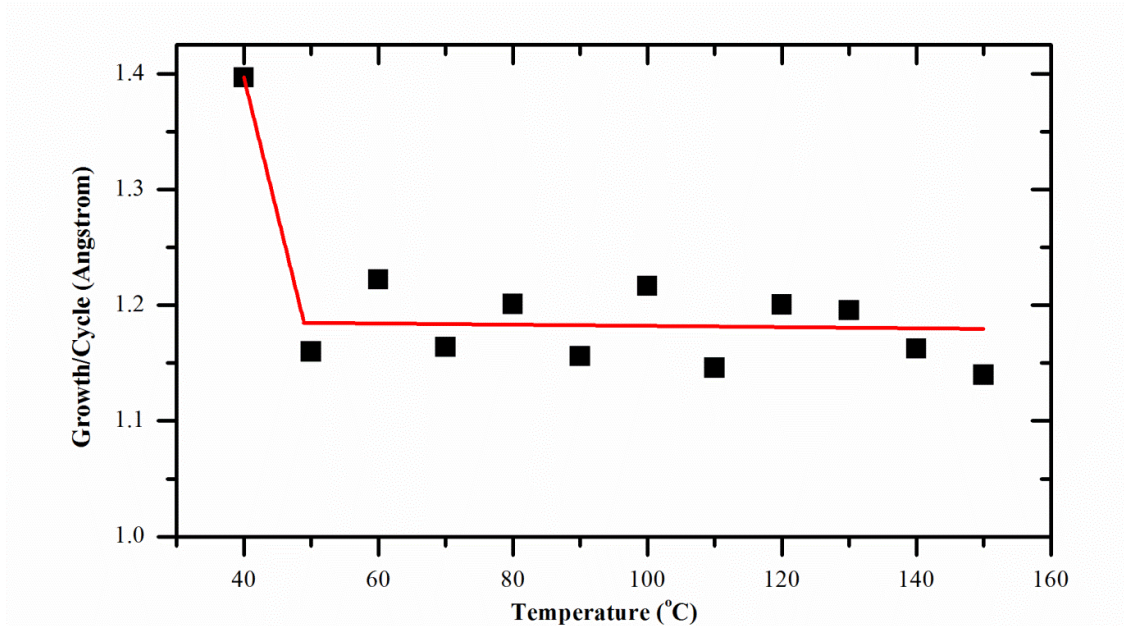


Figure 3.4. Temperature window of Al₂O₃ ALD of the reactor used in this study.

This data shows that the growth rate remains almost the same from 50 to 150 °C, being around $1.17 \pm 0.04 \text{ \AA} / \text{cycle}$. The growth rate is higher at 40°C because of the low kinetics of precursors at low temperature, leading to the condensation of TMA and water on the surface of substrates.

In this study, 60, 90 and 120 °C were chosen as the deposition temperature to investigate the temperature influence on the growth of alumina on polymers. 100 cycles ALD alumina was

deposited on spin cast PA-6 films and PSR-4000. 200 cycles ALD alumina was deposited on freestanding PA-6 films to get thicker coatings.

3.3 Microscopy Characterization Techniques

3.3.1 Transmission Electron Microscopy (TEM)

Transmission Electron Microscopy (TEM) is a microscopy technique where a beam of electrons are transmitted through an ultra-thin specimen. This beam interacts with the specimen as it passes through. Changes in electron density, phase and periodicity are observed.[72] By collecting and analyzing the secondary electrons, an image of the specimen is obtained. The resolution of a TEM is dictated primarily on the wavelength of electrons, allowing for atomic level resolution. The contrast of TEM images can be improved by decrease of electron energy. As the electrons need to transmit the sample, the thickness of TEM samples is required to be at most hundreds of nanometers.

As this study seeks to examine the interaction between the coatings and the polymer, cross-sectional transmission electron microscopy (TEM) was used. The cross-sectional samples were prepared by focused ion beam (FIB) processing using a FEI Quanta 3D FEG. For the FIB preparation, a thick layer of platinum was first deposited on a small rectangular area on the surface of the polymer. The materials around this area was etched away using platinum ion beam, leaving a thin slice material that contains the cross sectional features of the sample. The final step of the FIB was to thin the slice further using ion beam milling to get the required thickness of TEM samples. For polymer samples, a layer of palladium/gold was

coated on the surface prior to the process to prevent the diffusion of ion beam deposited platinum into the coating.

The TEM images were obtained using a Tecnai G² F30 S-Twin system in Sandia National Lab and a Hitachi HF-2000 system in Analytical Instrumentation Facility (AIF) at NCSU with an accelerating voltage of 300 kV and 200 kV, respectively. Each instrument is equipped with a cold field emission electron source. Energy-dispersive X-ray spectroscopy (EDX) on the Tecnai G² TEM system was used to produce an elemental analysis of the sample.

3.3.2 Atomic Force Microscopy (AFM)

Atomic force microscopy (AFM) is a type of surface scanning probe microscopy with resolution on the order of nanometer. It consists of a cantilever with a tip of nanometer radius that is used to scan the surface of specimen. When the tip is brought to the proximity of the sample surface, a force between the sample and the tip will be deflected by the force. As the tip is moved across the sample surface, topographical roughness will alter the distance between the tip and sample surface, resulting in a continuous change in the interfacial force. To maintain a constant force between the tip and the sample, the distance between them is adjusted continuously. The AFM images are generated by quantifying changing force between cantilever tip and the sample.[73] The imaging mode of AFM includes static mode (also called contact mode) and dynamic mode (non-contact or tapping mode).

In this study, AFM was used to observe the surface microstructure of samples and conformability of the alumina ALD coating. Most images were acquired using Veeco

Dimension 3100 AFM in tapping mode operation with a SiN NSC 15 Cantilever from Micromasch®. The system located at Sandia National Lab. The tip has a 10 nm radius, 325 kHz resonant frequency, and a 46N/m force constant. The oscillation amplitude was set to be 90% of the free oscillation during the test. The images of two samples (100 cycles ALD on PA-6 films at 90°C and PSR-4000 at 60°C) were obtained from AIF at NCSU using Digital Instrument D3000 AFM with silicon AC160TS cantilever from Olympus®. The cantilever has a 300 kHz resonant frequency and 26 N/m spring constant and the tip radius is 7 nm.

3.4 Mechanical Property Characterization Techniques

3.4.1 Nanoindentation

The hardness and Young's modulus of 100 cycles alumina films deposited on PA-6 and PSR-4000 was determined utilizing a commercial nanoindenter system (TI 900 TriboIndenter®, Hysitron) with displacement resolution of < 1 nm. The samples were indented using a diamond Berkovich tip and an increasing applied load from 5 to 150 μ N. Nanoindentation measurements were conducted in Quasi Mode, where the applied load and displacement of the tip were recorded continuously. The example curve obtained from one indentation is shown in figure 3.5.

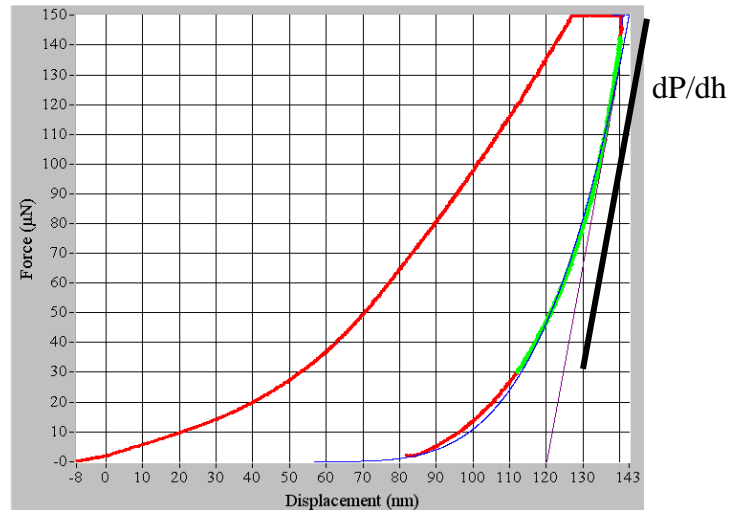


Figure 3.5. Example curve obtained from nanoindentation of a spun cast PA-6 film.

The curve consists of loading curve, holding curve at maximum load of 150 μN and unloading curve. The contact depth of the tip in this measurement is 125.8 nm. The hardness and combined elastic modulus were estimated by the data analysis software (Triboscan 8), which uses the Oliver and Pharr model to fit the unloading curve. At each load, three to five different indentations were obtained and averaged.

To interpret the properties of the ALD film, an extrapolation methods introduced in ISO14577-4[63] was incorporated. In this method, the extrapolation range for contact modulus and hardness was defined where contact depth was less than 50% of the total ALD coating thickness. Using this method, two extrapolation lines that represent the coating and the PA-6 properties, respectively (shown below) are obtained.

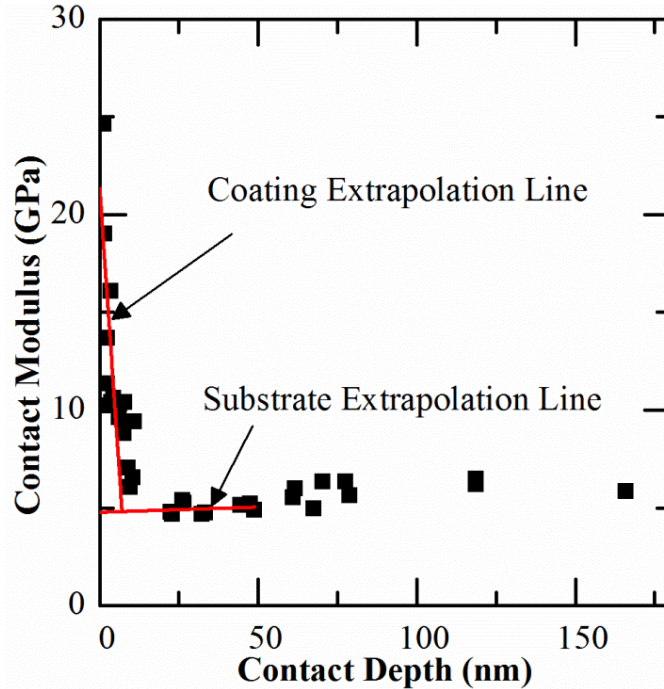


Figure 3.6. Extrapolation of contact modulus for ALD alumina deposited on PA-6 at 60 °C to zero contact depth.

For the samples analyzed in this work, this method was used to determine both the PA-6 and ALD thin film properties. As shown in figure 3.6, the intercept of coating extrapolation line on Y axis represents the contact modulus of ALD alumina films. This line was extrapolated from the measurements where the contact depth of the tip was less than 6.1 nm (50% of the total ALD alumina thickness). With the increase of the contact depth, the slope of the modulus or hardness versus contact depth plot changed as values rapidly approaching that of the PA-6. The extrapolating range for the substrate was defined where the contact depth was between 22.5 nm and 50 nm because when the contact depth was larger than 50 nm, the silicon underneath the PA-6 started to affect the nanoindentation results.

3.4.2 Bending Test

Bending testing was conducted on a flexible test apparatus as described in section 2.3.2. The original length between the two holders was set to be 20 mm. With the movement of two holders, the sample is bent into a cylindrical curve and the central region of the curvature was observed using optical microscopy (Nikon SMZ-10) equipped with the Lumenera® Infinity X-32C camera. In order to obtain a clear resolution of the cracks on the freestanding PA-6 films, 200cycles ALD were necessary. The displacement of the sample holders where the crack started was recorded and corresponding critical tensile strain of the coatings was calculated. The crack spacing, density and critical strain were evaluated at displacements (ΔL) of 6mm, 9mm and 12mm, corresponding to strains of 0.84%, 1.03% and 1.19%. Data is reported based on an average of three sample specimens.

4. ALUMINUM OXIDE DEPOSITION ON PA-6

4.1 TEM Analysis

The interface between ALD alumina and PA-6 was investigated using cross-sectional TEM analysis. Figure 4.1 provides images of PA-6 with alumina (100 ALD cycles) deposited at temperatures of 60, 90 and 120 °C. Before the FIB preparation, the Pd/Au coating was sputtered on the top of the samples to protect the ALD coating from contamination of platinum. In figure 4.1 (a), the layers from bottom to top are: PA-6, hybrid layer, ALD alumina coating, Pd/Au sputtered coating, electron beam deposited Pt and ion beam deposited Pt coating. Figure 4.1 (b) and (c) contain the same sputtered Pd/Au coating and Pt coating, but the thickness of each layer varies.

As exhibited in the figures, the deposited aluminum oxide layer was thin and conformal to the surface of substrates, and show similar thickness at the different deposition temperatures. No cracks or voids are observed in the aluminum oxide films. At 60 °C and 90 °C, an image contrast was observed in the PA-6 film close to the coating, indicating subsurface modification of the polymers. With the increase of temperature, the subsurface modification becomes thinner, and at 120 °C, no subsurface modification was observed. This layer corresponds to the formation of a hybrid material containing both PA-6 and Al₂O₃. [11]

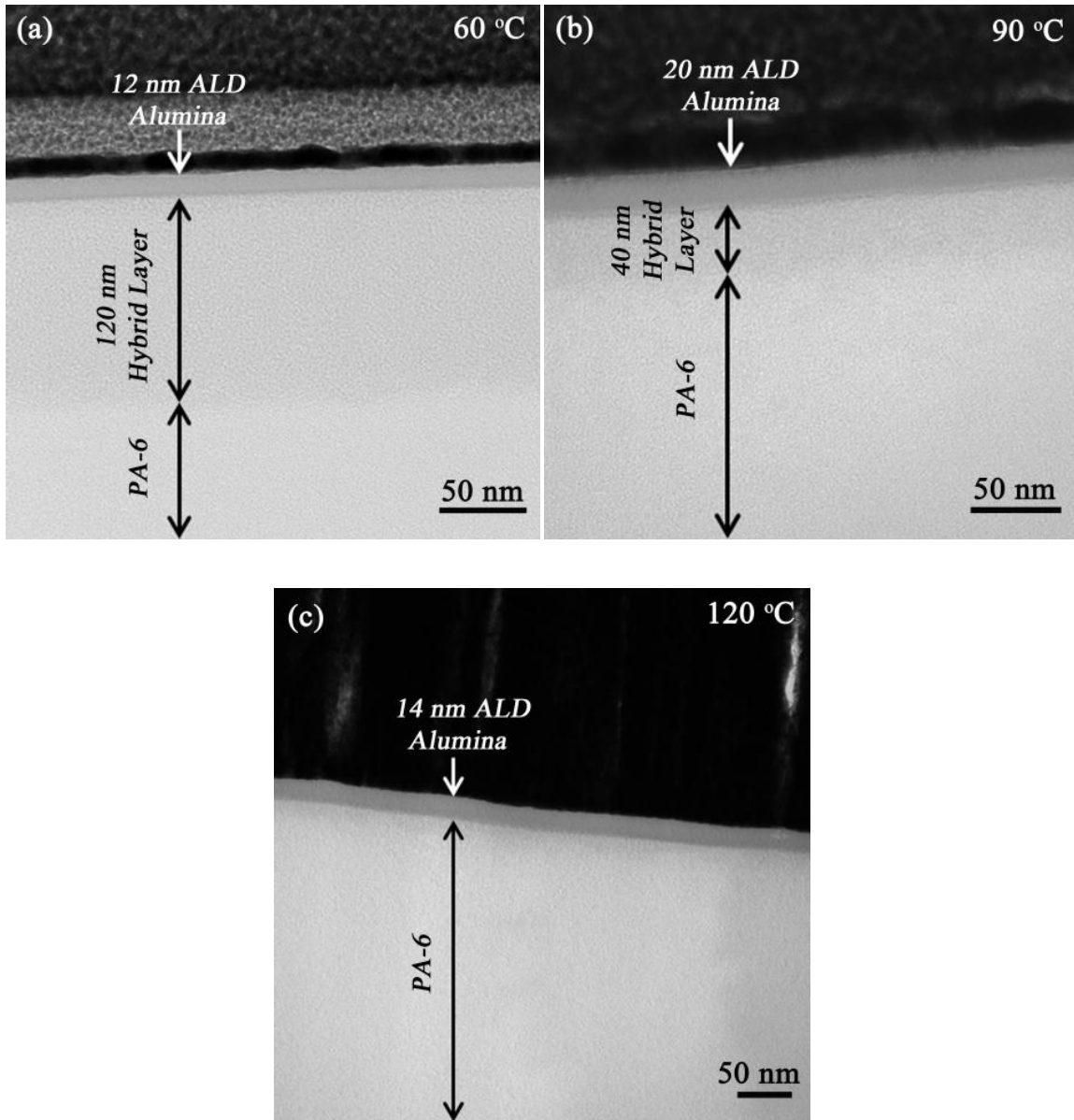


Figure 4.1. Cross sectional TEM images of 100 cycles Al_2O_3 ALD on spun cast PA-6 films at (a) 60 °C, (b) 90 °C and (c) 120 °C. (Figure (a) was observed under Tecnai G2 F30 S-Twin 300 kV TEM; (b) and (c) were observed under Hitachi HF 2000 cold Field Emission TEM)

Figure 4.2 shows the influence of dose time on the formation of hybrid layer. Longer dose time generated similar thick ALD alumina films on the surface of PA-6 but slightly thinner hybrid layer in the subsurface. Overall, longer dose time didn't lead to big difference to the samples that processed under short dose time.

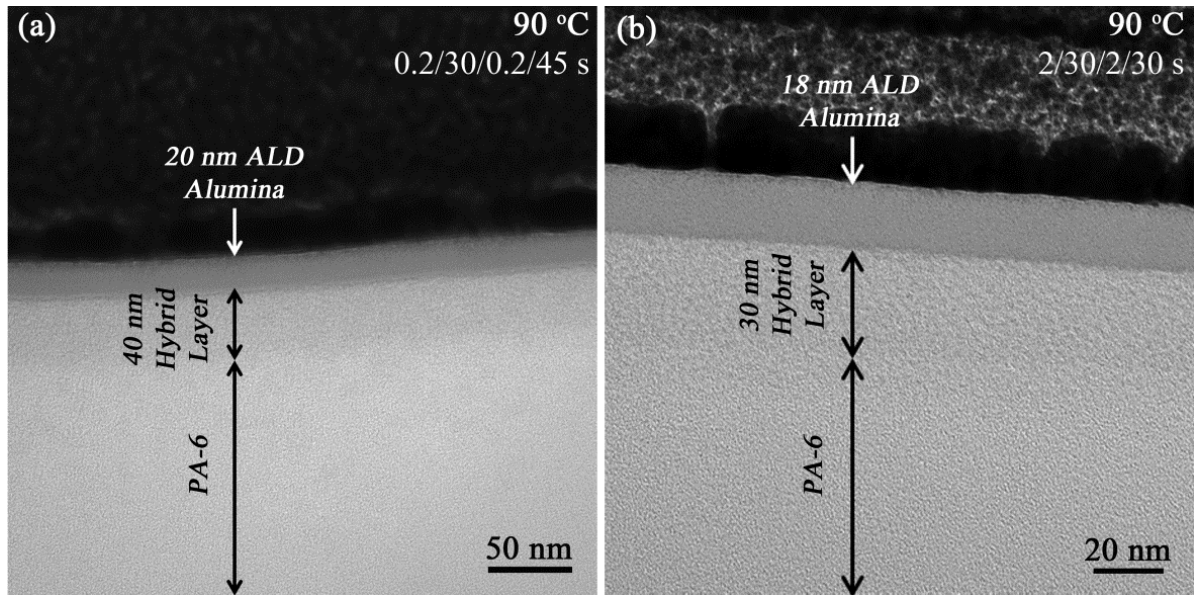


Figure 4.2. Cross sectional TEM images of PA-6 with 100 cycles Al_2O_3 ALD deposited at 90 °C with different dose time: (a) $\text{TMA}/\text{N}_2/\text{H}_2\text{O}/\text{N}_2 = 0.2/30/0.2/45\text{s}$ and (b) $\text{TMA}/\text{N}_2/\text{H}_2\text{O}/\text{N}_2 = 2/30/2/30\text{s}$.

To verify the elemental composition of the hybrid layer, the element mapping and energy-dispersive X-ray spectroscopy was performed on the sample processed under 60°C with 100 cycles alumina ALD.

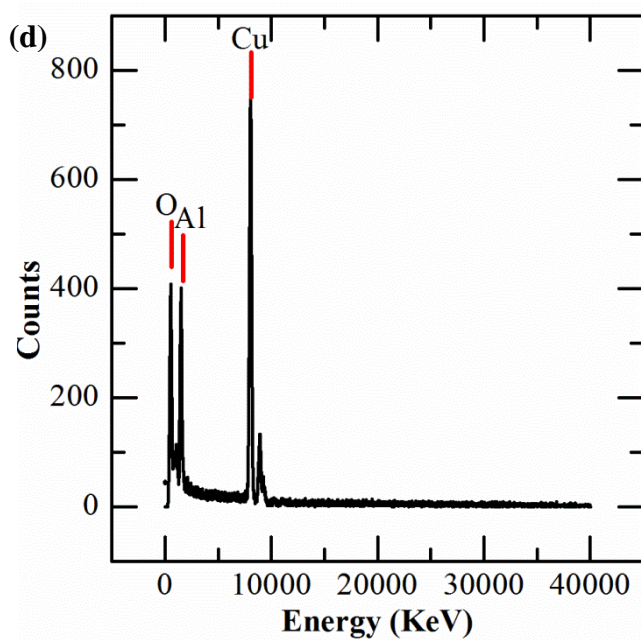
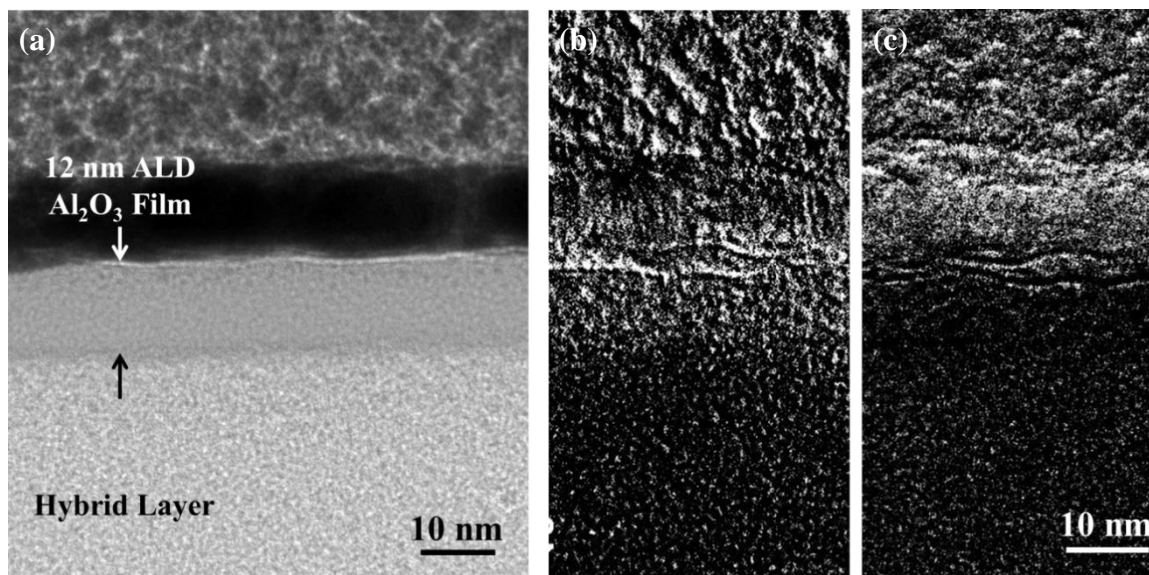


Figure 4.3. (a) TEM images of 100 cycles Al_2O_3 ALD on PA-6 films at 60 °C and (b) EDX mapping of aluminum and (c) gold. (d) EDX spectrum image of hybrid layer.

Figure 4.3(a) shows the high magnification TEM image of the specimen. Figure 4.3(b) is the aluminum map of the same position as in (a). The bright spots in hybrid layer display the distribution of the aluminum element. Figure 4.3(c) is the gold mapping of the specimen. It is used as a comparison image. Figure 4.3(d) provides the EDX spectrum image of the hybrid layer. The Al peak shown in the spectrum indicated the existence of aluminum in the hybrid layer, proving there was diffusion of precursors into polymer films. The Cu shown in the spectrum is the contaminant from sample grid which is made of copper.

The growth mechanism of ALD alumina on PA-6 can be proposed by analyzing its growth behavior described before. It is believed that the aluminum element in hybrid layers existed in two types: one was Al_2O_3 powder, generated by the diffusion of precursors into the polymer, and the other one was $-\text{C}-\text{O}-\text{Al}(\text{OH})_2$, formed by the reaction between TMA and carbonyl groups following a Grignard mechanism.[11] At higher temperature, reaction between TMA and carbonyl group was enhanced because of high kinetics. Most precursors that diffused into the polymer reacted with the functional group on polymer chains, preventing the further diffusion of precursors. This is why the decreasing hybrid layer was observed with increasing process temperatures.

The difference in hybrid layer thickness could also be explained by the density difference of Al_2O_3 layer at the first several cycles. It has been proved that the density of ALD alumina increases with an increase in deposition temperature.[4] At higher temperature, the Al_2O_3 formed from first several cycles was more compactly arranged. The dense layer prevented further diffusion of TMA into nylon 6 in the following cycles.

The reduction in hybrid layer after longer dose time can be explained by the enhanced reaction between TMA and carbonyl group. When the dose time was longer, more TMA was pulsed into the reactor in the first several cycles and more carbonyl groups were reacted. Then the prevention to the precursor diffusion into the polymer was improved and thinner hybrid layer was obtained. Spagnola et al.[11] investigated the cross-sections of PA-6 fibers after prolonged TMA precursor soaks (60 sequential steps of 1 minute each) followed by water exposures (20 steps of 1 minute each). The dense hybrid layer proved that large amount of carbonyl groups would react with precursors under long exposure time.

4.2 AFM Analysis

To analyze the surface microstructure change of the samples after ALD processing, AFM was used. Figure 4.4(a)-(d) presents representative AFM images of the spun cast PA-6 films before and after 100 cycles ALD aluminum oxide processing. For all films, the granular appearance represents the crystals on the surface of the PA-6, and can provide some information as the effect the ALD coating has on the near surface polymer crystals.

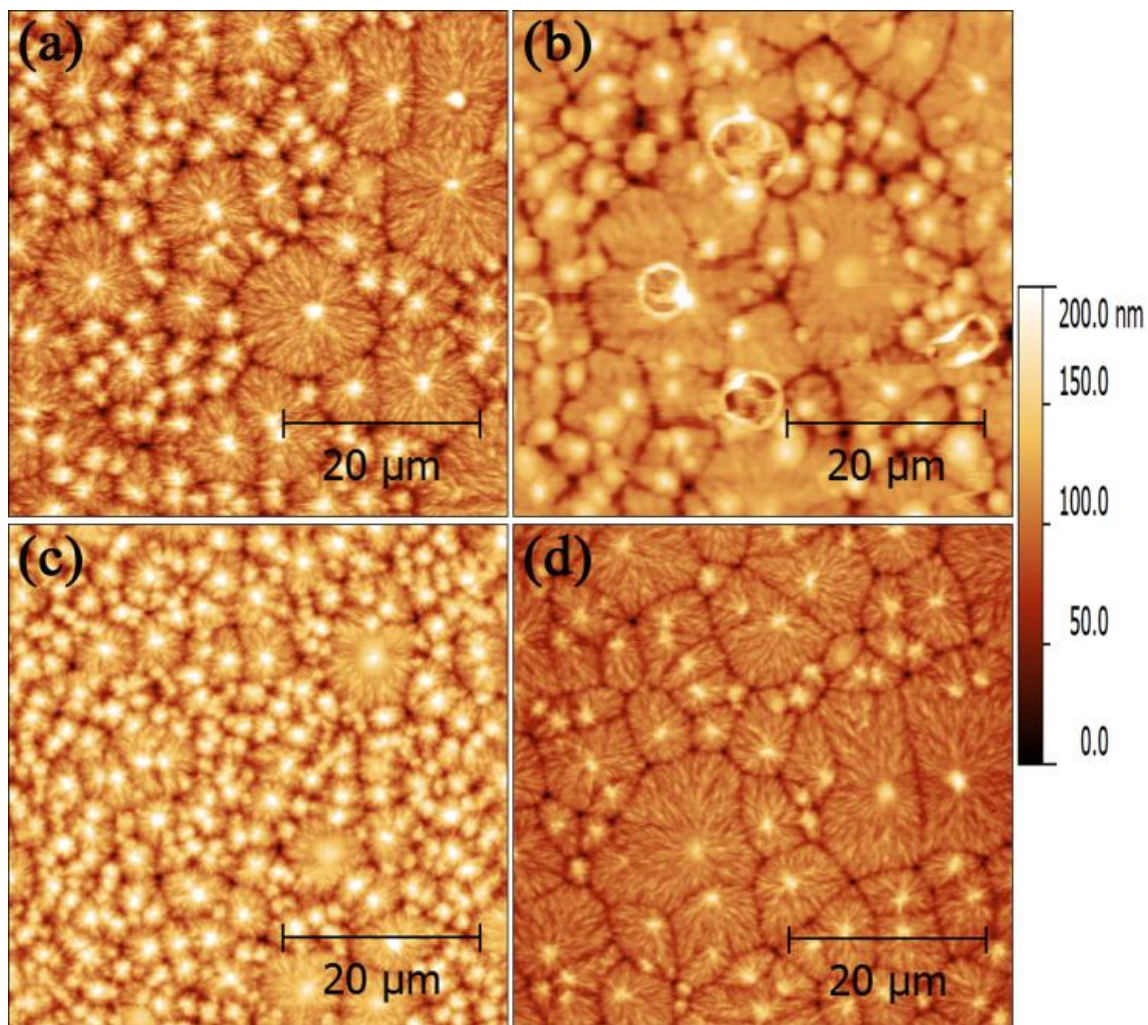


Figure 4.4. AFM surface images of (a) PA-6 and PA-6 with 100 Al₂O₃ ALD cycles deposited at (b) 60 °C, (c) 90 °C, and (d) 120 °C.

In figure 4.4(a), the average grain size of spun cast PA-6 film is $5.74 \pm 3.21 \mu\text{m}$. After ALD alumina processing at 60 °C, the grain size of the sample is 5.28 ± 2.98 , as shown in figure 4.4(b). In figure 4.4(c) and (d), the grain size of the sample after ALD growth at 90 °C and 120 °C are $4.03 \pm 1.64 \mu\text{m}$ and $6.65 \pm 3.37 \mu\text{m}$, respectively. No big difference in grain size

between samples was observed. The AFM images also prove that the ALD alumina coating is conformal to the surface of the polymer.

All AFM images only provide an analysis of a small part on the samples. When we focused on other positions, different surface topography was observed on the sample processed under 60 °C, but the other three samples showed the similar result.

Figure 4.5 displays a circular blister on the surface of PA-6 processed under 60 °C. The blister indicated the delamination between alumina coating and PA-6 substrate at some point. Similar blister has been observed on 200 nm thick nickel films sputtered on polycarbonate substrate, which was attributed to the high internal compressive stresses developed during deposition process.[74] For the delamination happened on PA-6 films processed at 60 °C, the residual compressive stress is not the main reason because no blister was found on films processed at higher temperatures, in which higher residual stress existed.

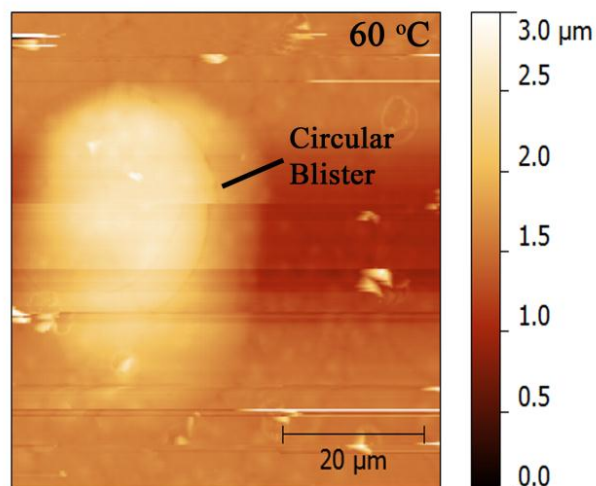


Figure 4.5. Circular delamination point on PA-6 films with 100 cycles Al_2O_3 ALD deposited at 60 °C.

To investigate the source of the delamination, AFM analysis was performed at an increased magnification. Figure 4.6(a)-(c) shows the high magnified AFM images of the ALD films deposited on PA-6. In figure 4.6(a), processing at 60 °C showed smoothening of the PA-6 film surface and evidence of nanoscale-pin hole that features 3-5nm in depth. In comparison, the films after ALD processing at 90 °C and 120 °C showed the similar surface topography as the virgin film.

The pin holes indicated in fig. 4.6(a) may be the cause of the delamination on PA-6 after processing at 60 °C. The delamination usually happened after the sample was taken out of the chamber for one or two days. During this period, the moisture in the atmosphere might diffuse into the polymer through the nano-scale pin holes on the surface of ALD alumina coating, and then lead to the delamination between the polymer and the ALD coating.

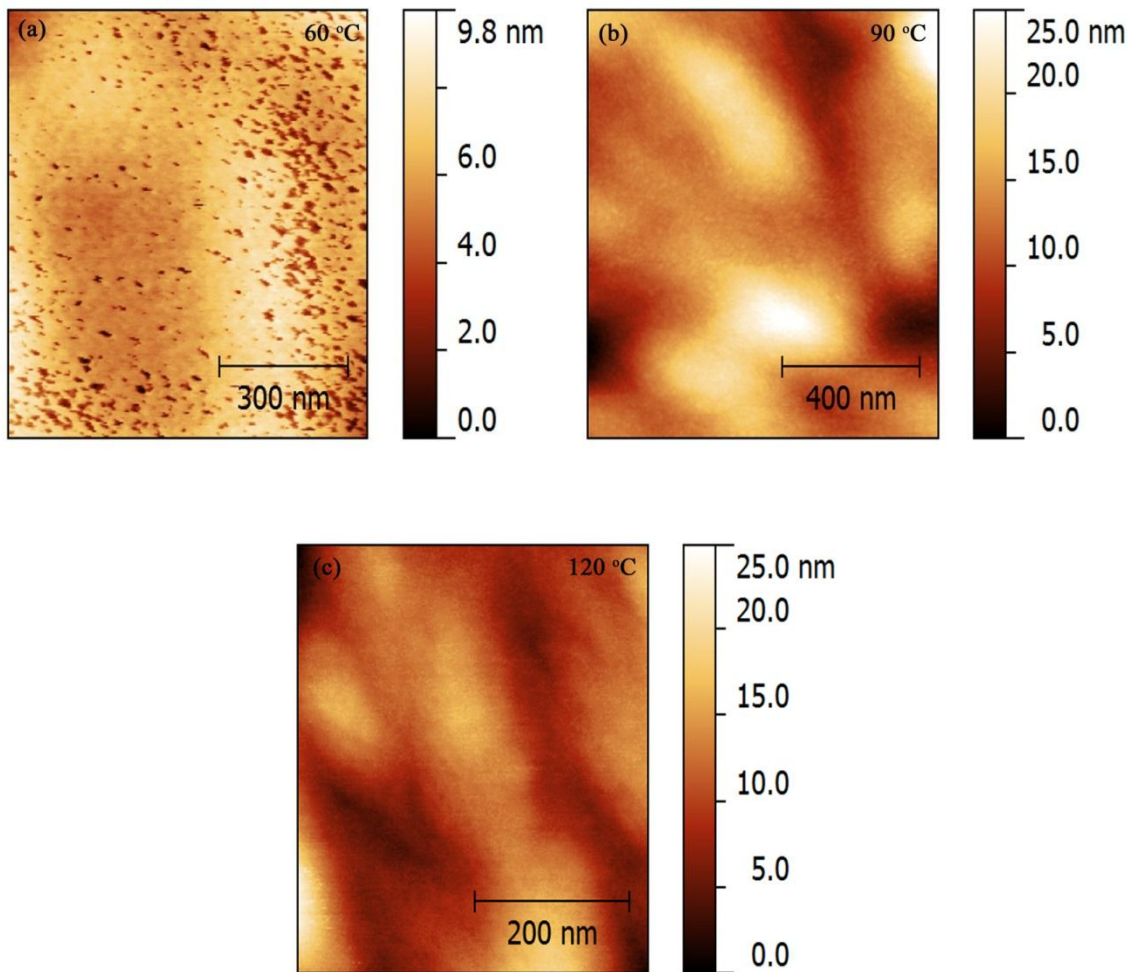


Figure 4.6. Magnified AFM images of PA-6 with 100 Al₂O₃ ALD cycles deposited at (a) 60 °C, (b) 90 °C, and (c) 120 °C.

The influence of dose time on the microstructure of PA-6 processed with ALD under 90 °C was also investigated. The cycle time performed on samples shown in Figure 4.7(a) and (b) is 0.2/30/0.2/45s and 2/30/2/30s, respectively. No difference in grain size was observed.

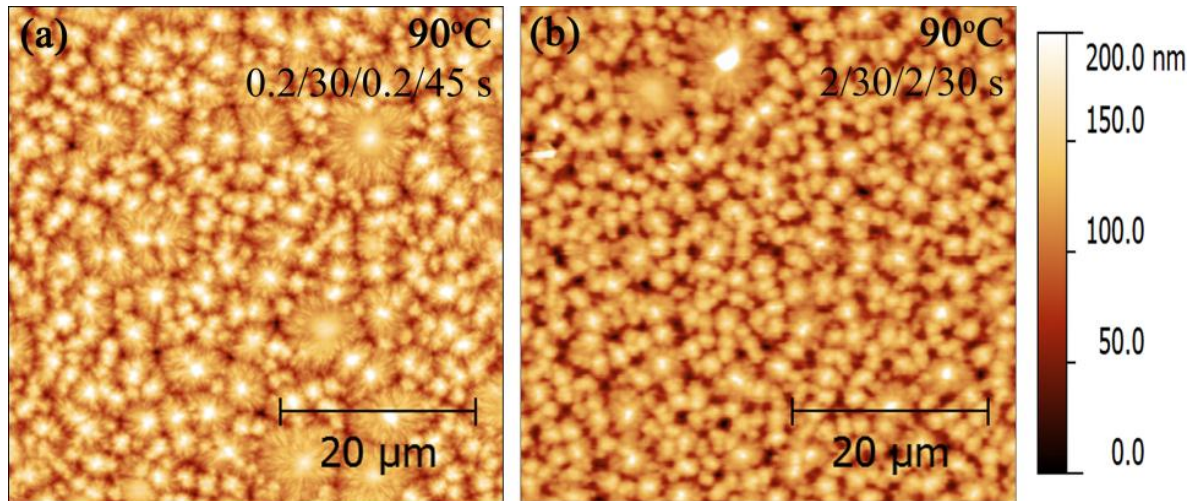


Figure 4.7. AFM surface images of PA-6 with 100 cycles Al₂O₃ ALD deposited at 90 °C using different dose time: **(a)** TMA/N₂/H₂O/N₂ = 0.2/30/0.2/45s and **(b)** TMA/N₂/H₂O/N₂ = 2/30/2/30s.

4. 3. Mechanical Analysis

Nanoindentation was used to investigate the modulus and hardness of ALD alumina coating on spun cast PA-6. Then the Bull's model [18] was imported to predict the modulus of ALD Al₂O₃ coating on PA-6 with no existence of hybrid layer. Through comparing the predicted data and experimental data, we could understand the hybrid layer effect on the mechanical properties of ALD alumina coating.

When nanoindentation is used to measure the coating-only properties on a coating/substrate sample, a commonly used rule of thumb is to control the indentation depth to less than 10% of the whole film thickness.[17] In this study, the thickness of ALD alumina coatings on PA-6 was just more than ten nanometers. The rule introduced above can't be used to obtain the properties of ALD alumina coating. ISO14577-4 standard was used to extrapolate the contact

modulus and hardness of the ALD coatings. Figure 4.8 shows the measured contact modulus and hardness of the virgin spin cast PA-6 films as compared to PA-6 films with 100 cycles ALD coating grown at different temperatures.

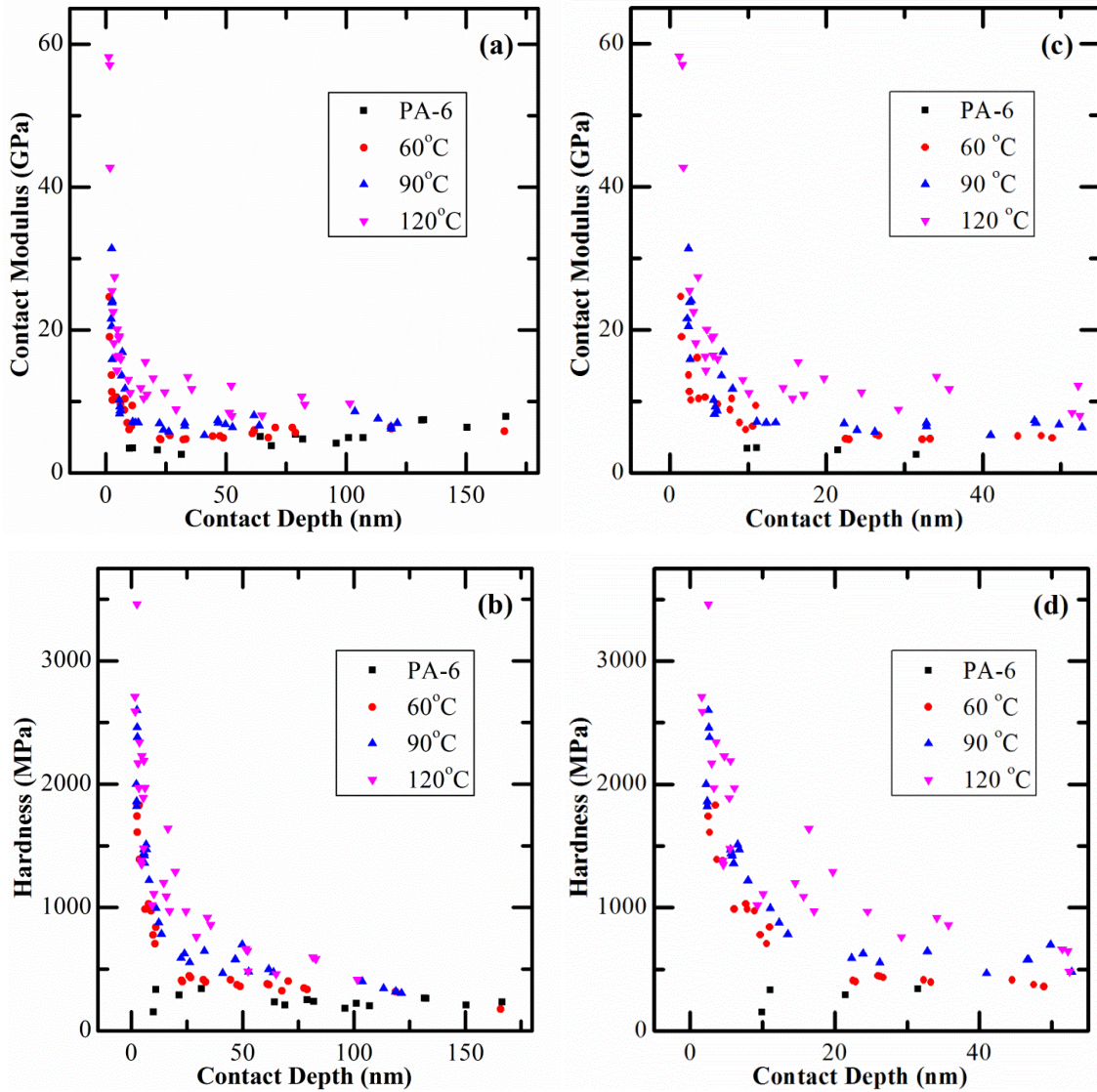


Figure 4.8. Variation of (a) contact modulus and (b) hardness vs. contact depth for virgin PA-6 films and PA-6 with 100 cycles Al_2O_3 ALD coatings. (c) and (d) are the same plots zoomed into 55 nm contact depth.

From Fig. 4.8 (a), we can see that when the contact depth into PA-6 was larger than 60nm (~10% of the whole PA-6 film thickness), the silicon substrate underneath the PA-6 began to influence the elastic modulus measurement. The same trend was observed on other samples with an increase in contact depth. In Fig. 4.8(b), the indentation hardness changed little at high contact depth, indicating the silicon effect on hardness of the samples was not as obvious as on elastic modulus. In all four figures, a sharp decrease in the elastic modulus and hardness of alumina coatings was observed when the contact depth was less than 50nm because of the effect of soft PA-6 films under aluminum oxide coating

The extrapolated contact modulus and hardness of the PA-6 coated and uncoated were listed in Table 3. The density of ALD alumina coatings at different temperatures was obtained from the literature.[4] The elastic modulus of alumina films were calculated using the following equation:

$$\frac{1}{E_r} = \frac{1 - \nu_i^2}{E_i} + \frac{1 - \nu_s^2}{E_s}$$

For the Berkovich tip used in the experiment, $E_i = 1140$ GPa and $\nu_i = 0.07$. An estimate of $\nu_s = 0.24$ was made for the amorphous alumina coating.

In Table 3, both the modulus and hardness of ALD alumina coating on PA-6 shows an increase with an increase in deposition temperature. According to the literature, the density of the ALD coating deposited at different temperature also varies and shows an increasing trend with the temperature.

Table 3. Extrapolated contact modulus and hardness, calculated elastic modulus and density of ALD alumina coatings on PA-6.

Deposition Temperature (°C)	Alumina Contact Modulus (Gpa)	Alumina Hardness (Gpa)	Elastic Modulus (Gpa)	Density ^[4] (g/cm ³)
60	21.32 ± 3.22	2.25 ± 0.17	20.47 ± 3.04	2.5 -- 2.75
90	28.40 ± 3.38	2.62 ± 0.19	27.44 ± 3.19	2.6 -- 2.82
120	55.80 ± 6.00	3.22 ± 0.39	55.28 ± 5.68	2.8 -- 3.10

The variation in modulus and hardness of alumina coating could be attributed to the intrinsic structure difference of ALD coatings. The alumina coating deposited at low temperature had a lower density because of high hydration concentration in the films,[4] which may weaken the atomic bonding of the film and exhibits a decrease in elastic modulus. It also explains the increasing elastic modulus of the ALD alumina thin coatings deposited on silicon with increasing deposition temperatures (see Table I).

The extrapolated values are lower than the reported contact modulus of ALD alumina films that are usually between 160 to 220GPa.[13-15, 18] The low measured contact modulus is due to the low stiffness of PA-6 substrate. The modulus mismatch between the coating and substrate made it difficult to obtain reliable data. For hard thin coatings on soft substrates, Bull[18] created a model to predict the variation in contact modulus of the coating as a function of contact depth.

Bull's model is based on a truncated cone of load support beneath the coating.[18] The basic equation for the calculation of the elastic modulus is defined as,

$$E = \frac{P}{2a_0(\partial_c + \partial_s)}$$

where P is the indentation load and a_0 is the radius of the contact area (for a Berkovich indenter, $a_0 = h_c\sqrt{24.5/\pi}$). ∂_c and ∂_s are displacements in the coating and substrate. They are given as:

$$\partial_c = \frac{P}{\pi E_c} \left[\frac{1}{a_0 \tan \alpha} - \frac{1}{a_0 \tan \alpha + t_c \tan^2 \alpha} \right]$$

$$\partial_s = \frac{P}{\pi E_s} \left[\frac{1}{a_0 \tan \alpha + t_c \tan^2 \alpha} - \frac{1}{a_0 \tan \alpha + (t_c + t_s) \tan^2 \alpha} \right]$$

where E_c and E_s are elastic modulus of the coating and substrate, t_c and t_s are the thickness of the coating and substrate, α is the semi-angle of the cone of material supporting the load. This angle is 32.48° and is independent of the indenter geometry.

This is a model to describe a two-layer system, while the samples investigated in this work are not precisely two layer systems due to the hybrid layer formation in the subsurface of substrates. So Bull's model was used to predict the contact modulus of ALD alumina on PA-6 when there is no hybrid layer. The contact modulus obtained using the model is plotted in comparison to the experimental data in Fig. 4.9.

For samples processed at 120°C , the predicted data and experimental data matched well at each contact depth. But for sample processed under 60 and 90°C , the predicted results are consistently lower than the measured data, particularly at lower contact depths. The difference between the predicted contact modulus and experimental data can be attributed to the hybrid layer between the coating and the substrate. The hybrid layer contains both

aluminum and polymer components, and is harder than the polymer substrate, leading to the larger contact modulus during the measurement. Therefore it is natural to predict that the model will underestimate the contact modulus of samples that contain the hybrid layer.

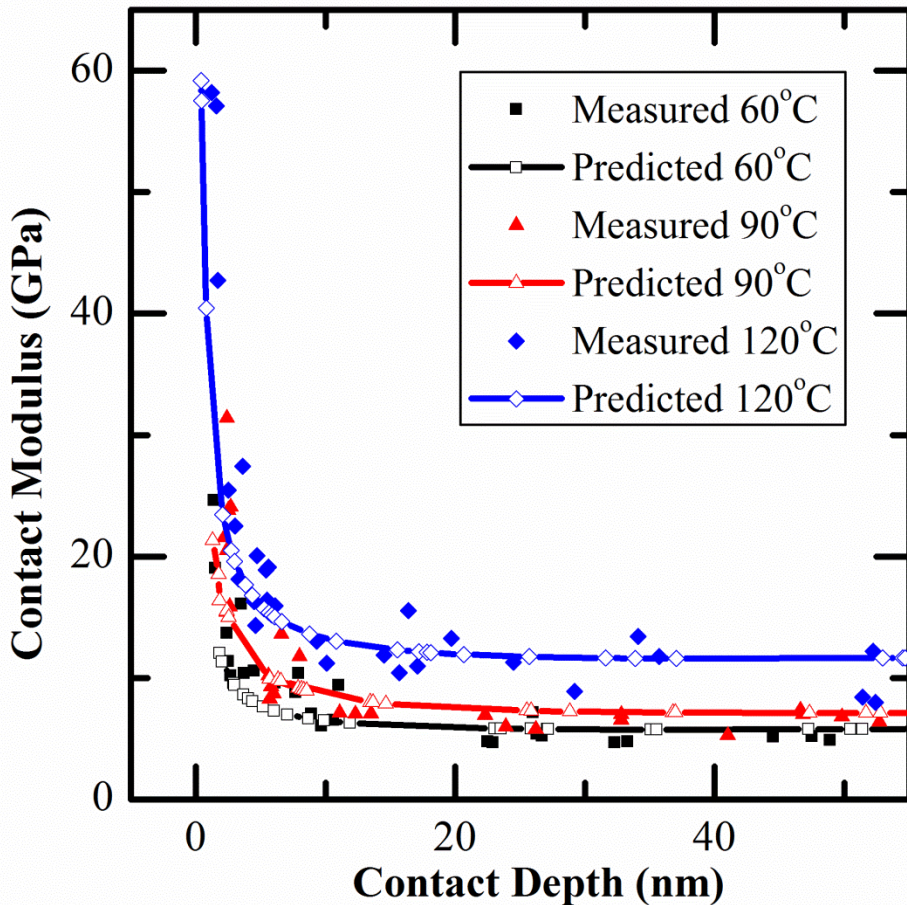


Figure 4.9. Predicted contact modulus for ALD alumina on PA-6.

In order to evaluate the properties of the hybrid layer, an ‘effective substrate modulus’ can be predicted that allows for a fitting of the model to the experimental data. The effective substrate modulus replaced the E_s in the function of ∂_s given by Bull’s model. Different values were tried for effective substrate modulus until good fitting between predicted data

and experimental data was achieved. Figure 4.10 presents the predicted contact modulus obtained from modified model and measured contact modulus. The two data sets match very well without regard to the scatter of the experimental data. At smaller contact depths, the effective substrate modulus is higher because of the high modulus of hybrid layer. With the increase of contact depth, effective E_s decreased to the substrate modulus because the PA-6 dominates the whole system.

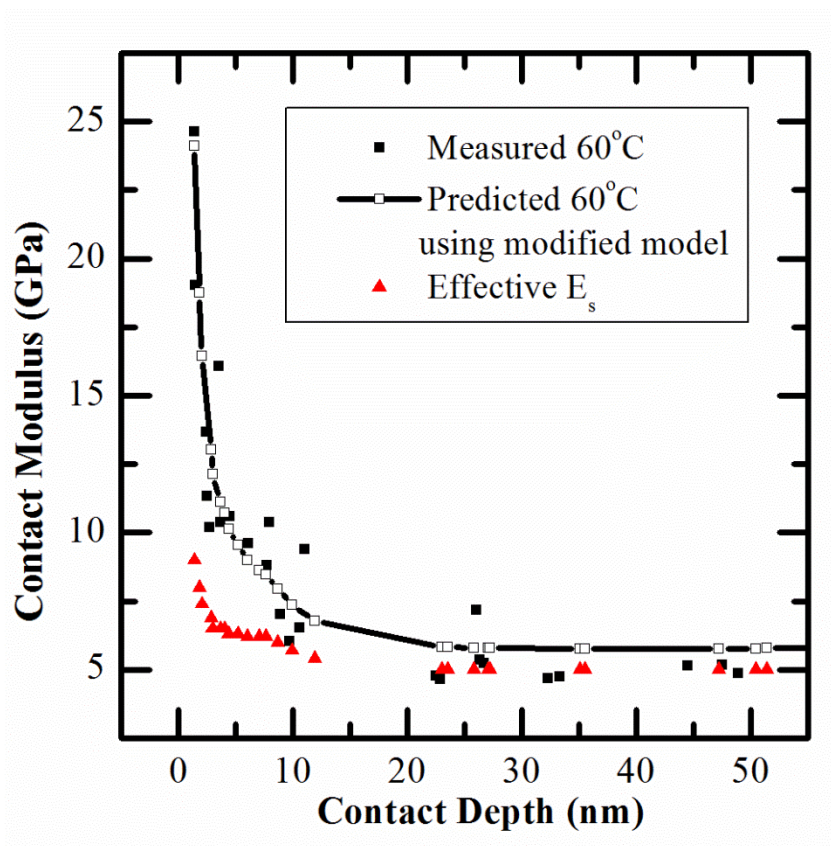


Figure 4.10. Predicted contact modulus of 100 cycles ALD alumina on PA-6 grown at 60 °C after model adjustment.

It is important to note anomalies observed in the nanoindentation process. By analyzing the load-displacement curve recorded during the penetration process, it is found that when the applied force increased to a certain value, there was a sharp increase in the displacement of the tip (pop-in events), as is shown in Figure 4.11.

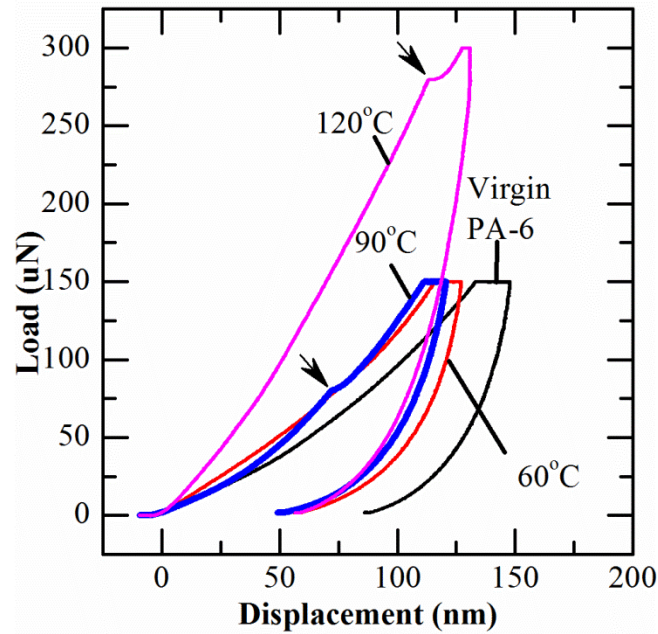


Figure 4.11. Load-displacement curve of PA-6 and PA-6 with alumina processed at 60, 90 and 120 °C. Pop-in events are indicated by the arrows.

There was no pop-in event on PA-6 processed at 60°C. The pop-in on PA-6 processed under 90°C happened when the displacement was around 75nm. For PA-6 coated with 100 ALD alumina cycles at 120°C, the pop-in happened when the displacement was 100nm.

This phenomenon is usually attributed to the dislocation nucleation and propagation, or micro-cracking.[75] Reverse discontinuities on the unloading curve, or pop-outs, have been

observed on Si and are attributed to the undensification of the silicon substrate, residual deformation of the thin films, or pressure-induced phase transformation.[76] No evidence of pop-outs was observed in the samples investigated in this work.

The pop-ins during nanoindentation performed in this study might be caused by the crack of the aluminum oxide coating. The pop-ins could also be used as a measurement of flexibility of different films because the alumina coatings cracked at a larger displacement were more flexible than those cracked with small deflection.

4.4. Bending Test

The bending test was performed on the freestanding PA-6 films with 200 cycles ALD Al_2O_3 coating. The critical tensile strain of ALD alumina coatings grown under different temperatures was recorded. The crack density and crack spacing on alumina coatings was also plotted as a function of tensile strain to better understand the fracture behavior of ALD alumina coatings on PA-6.

During the bending process, since the highest tensile strain is located at the center point of the film bending, the cracking behavior of ALD coatings was investigated here in the following studies. The distribution of the strain at the top of curvature is believed to be uniform. Figure 4.12 depicts the cracking of the 200 cycles ALD Al_2O_3 coatings grown on freestanding PA-6 films under increasing applied tensile strain. A minimum of 200 cycles ALD was applied on the polymer films in order to obtain clear crack resolution during the testing.

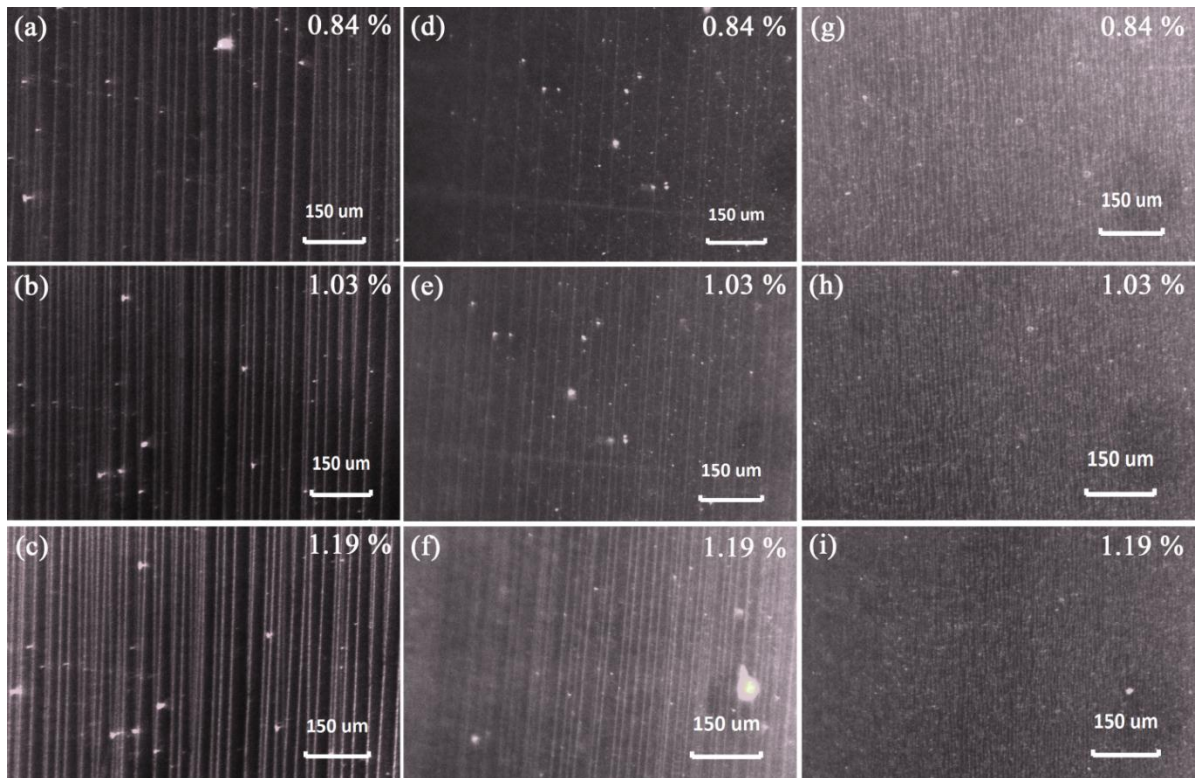


Figure 4.12. Representative optical micrographs of the cracked alumina thin films processed at 60 °C (a)-(c), 90 °C (d)-(f) and 120 °C (g)-(i) for 200 cycles. The corresponding strain values are indicated on the top of image.

Figure 4.12 shows that for one sample, the number of parallel cracks increases with the increasing applied strain. A critical strain can be evaluated as the point at which cracks first appears. Once the applied strain exceeds the critical strain, parallel cracks perpendicular to the tensile strain direction were observed. The critical strain of alumina coatings was found to be different when the deposition temperature varies from 60 °C to 120 °C. Figure 4.13 presents the critical strain of the three different samples and the corresponding displacement ratio of the sample holder ($\Delta L/L$).

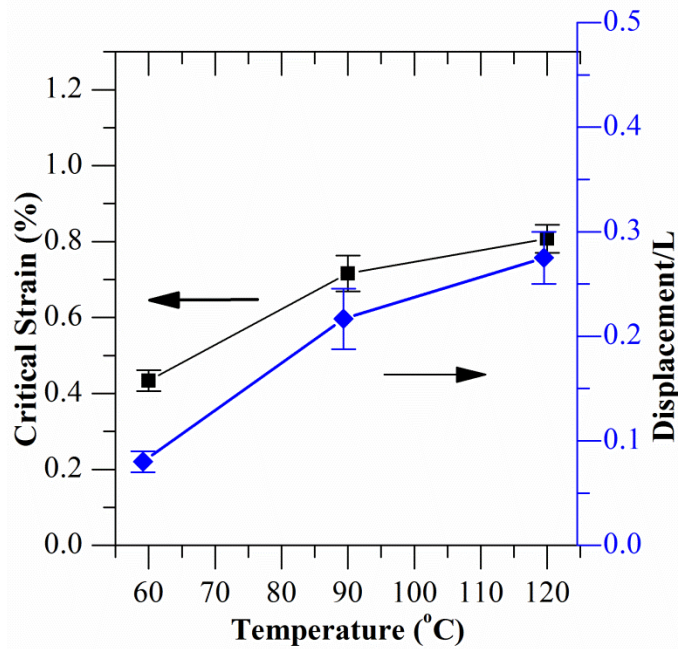


Figure 4.13. Crack initiating critical strain of 200 cycles alumina films processed at 60, 90 and 120 °C.

The alumina coating deposited at higher temperature had a higher critical tensile strain, meaning a much higher tensile stress was needed to fracture the coating grown at higher temperature. The flaws in the coatings could also affect their critical tensile strain.[59] As observed in the AFM images, there were pin holes on the surface of alumina coating grown at 60 °C, as well as delamination between the coating and polymers. Both the pin-holes and delaminations may enhance the crack initiation in the films. Under small tensile stress, those pinholes might grow to cracks that traverse the full width of the samples.

For the sample processed under 120 °C (figure 4.12(g)-(i)), the initiated cracks were of a high density and additional crack densification was not obvious with increased strain. I The

quantitative results of the bending test are shown in Figure 4.14 that plotted the average spacing between cracks and crack density as a function of applied strain from 0-1.2%.

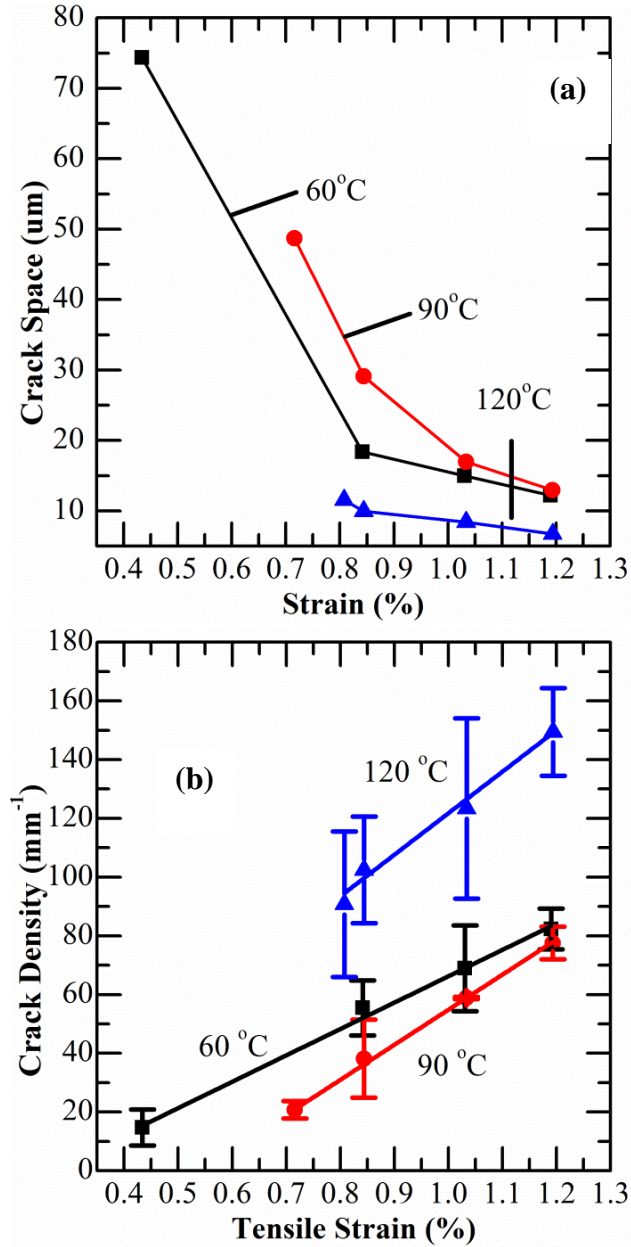


Figure 4.14. (a) Crack spacing and (b) crack density vs. tensile strain on the top of the bending curvature for 200 cycles alumina films processed at 60, 90 and 120 °C.

For sample processed at 60 °C, the average crack spacing is 74 μm and reduces to 12 μm at strain of 1.19%. The crack spacing on samples processed at 90 °C also changed from 49 μm to 13 μm with an increase in strain. Little change in crack spacing was observed on samples processed at 120 °C although the crack density also increased linearly, attributing to the high crack density at the critical strain.

The crack density shown in Figure 4.14(b) is around 150/mm for PA-6 processed under 120 °C and 80/mm for sample processed under 60 and 90 °C. Both values are far from the saturation density which is around 400 for 25nm thick Al₂O₃ ALD coating on HSPEN grown under 155°C.[64] From the study of Jen[64] and Mohanty[61], it can be known that the crack density of thin films changes linearly at the early age of bending test where the applied tensile strain is small. So the crack density in Figure 4.14(b) increases linearly.

The crack growth on different samples can be correlated to the interaction between Al₂O₃ ALD coating and polymer substrate. When processed under 60 and 90 °C, a hybrid layer is observed in the subsurface of the polymer. The hybrid layer might be able to slow down the growth rate of cracks on the Al₂O₃ coating, because the hybrid layer contained both polymer chains and aluminum element and forms a transition area between alumina coating and PA-6. The energy released by the formation of cracks can be transferred to the polymer substrate effectively by the hybrid layer or be contained in the hybrid layer. To initiate a new crack, external force energy is needed. In samples processed under 120 °C, there was no hybrid layer. The released energy will be transmitted within the alumina coating. The

transmitted energy provides the energy needed to induce new cracks, leading to high crack density at critical strain.

4.5 Conclusion

The growth mechanism of ALD Al_2O_3 on PA-6 can be proposed through analyzing the growth behavior of alumina coating on spun cast PA-6 films at different temperatures. There are two growth mechanisms happened at the same time: diffusion of precursors into PA-6 and reaction between precursors and PA-6. At low temperature, most precursors diffuse into the polymer and little react with the polymer chain. At high temperature, more precursors react with the polymer. The reaction between the polymer and precursors will prevent further diffusion of precursors, resulting in a thinner hybrid layer than the sample processed at low temperature. The delamination between the PA-6 and ALD alumina coating was observed on sample processed at 60 °C. While on the other samples, the ALD coating is conformal to the PA-6.

The elastic modulus and hardness of ALD alumina coating on PA-6 show an increasing trend with the increase of deposition temperature. It can be attributed to the intrinsic difference in coating structure. The hybrid layer between the coating and the substrate increases the contact modulus of the ALD alumina coating, and at the same time, it decreases the crack growth rate during the bending testing. The coating deposited at high temperature has a high critical strain.

5. ALUMINUM OXIDE DEPOSITION ON PSR-4000

5.1 TEM Analysis

The cross-section TEM images of PSR-4000 with 100 cycles ALD are shown in figure 5.1(a)-(c), where a conformal alumina layer was observed. There was no hybrid layer in the subsurface of PSR-4000 after ALD process, meaning no precursors diffused into the substrate during the deposition. But the thickness of alumina coatings obtained under 60 °C and 90 °C were as high as 100nm and 70nm, respectively, indicating the growth of the alumina coating was not in the atomic layer control.

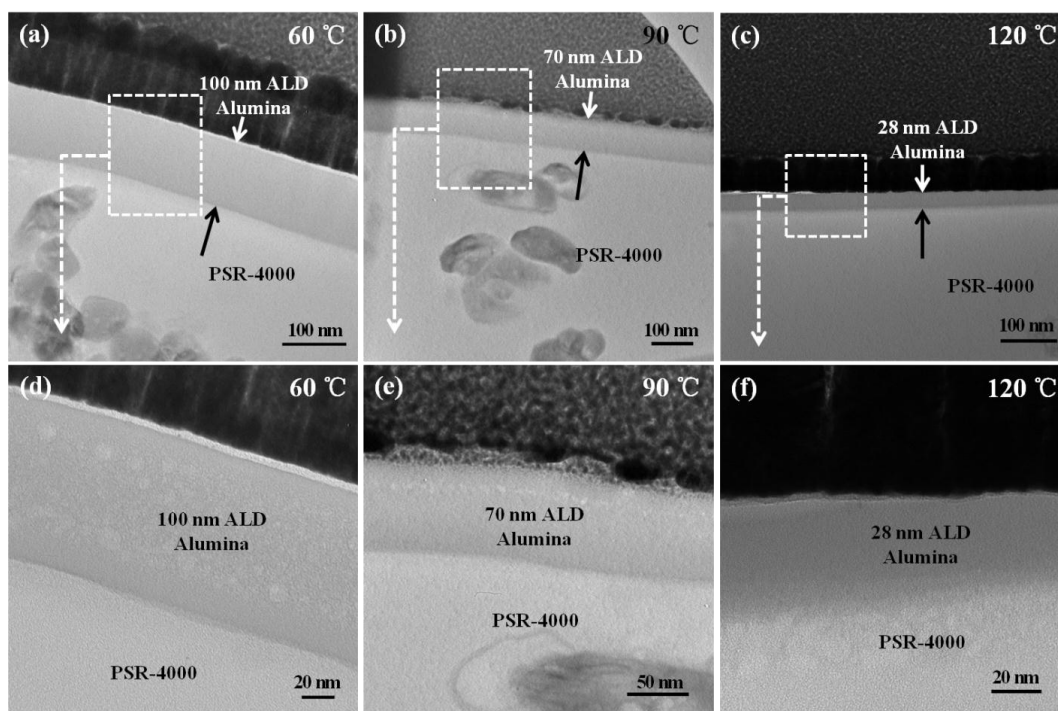


Figure 5.1. Cross sectional TEM images of 100 cycles Al_2O_3 ALD on PSR-4000 sheets at (a) 60 °C, (b) 90 °C and (c) 120 °C. The higher resolution images (d)-(f) show the microstructure of the alumina coating.

Figure 5.1(d)-(f) shows the magnified TEM images. In Fig. 5.1(d) and (e), the alumina layer grown under 60 °C and 90 °C contains some voids in the middle of the coating and more voids are observed in the thicker coatings. No voids were observed in the coatings processed at 120 °C.

5.2 AFM Analysis

The representative AFM images of PSR-4000 and PSR-4000 with 100cycles Al_2O_3 ALD are presented in figure 5.2. The surface of PSR-4000 was very rough with various holes on it and the alumina coating didn't change the morphology of surface effectively, but might cover some small defects. The coverage of alumina coatings deposited at 60 and 90 °C were better than that grown at 120 °C where a lot of small holes were still left. The holes on the surface of PSR-4000 might lead to moisture diffusion into the substrate when the sample is exposed to the ambient environment for a long time. So thicker inorganic layer or combination of different encapsulation methods are needed to further increase the water barrier properties of printed circuit board.

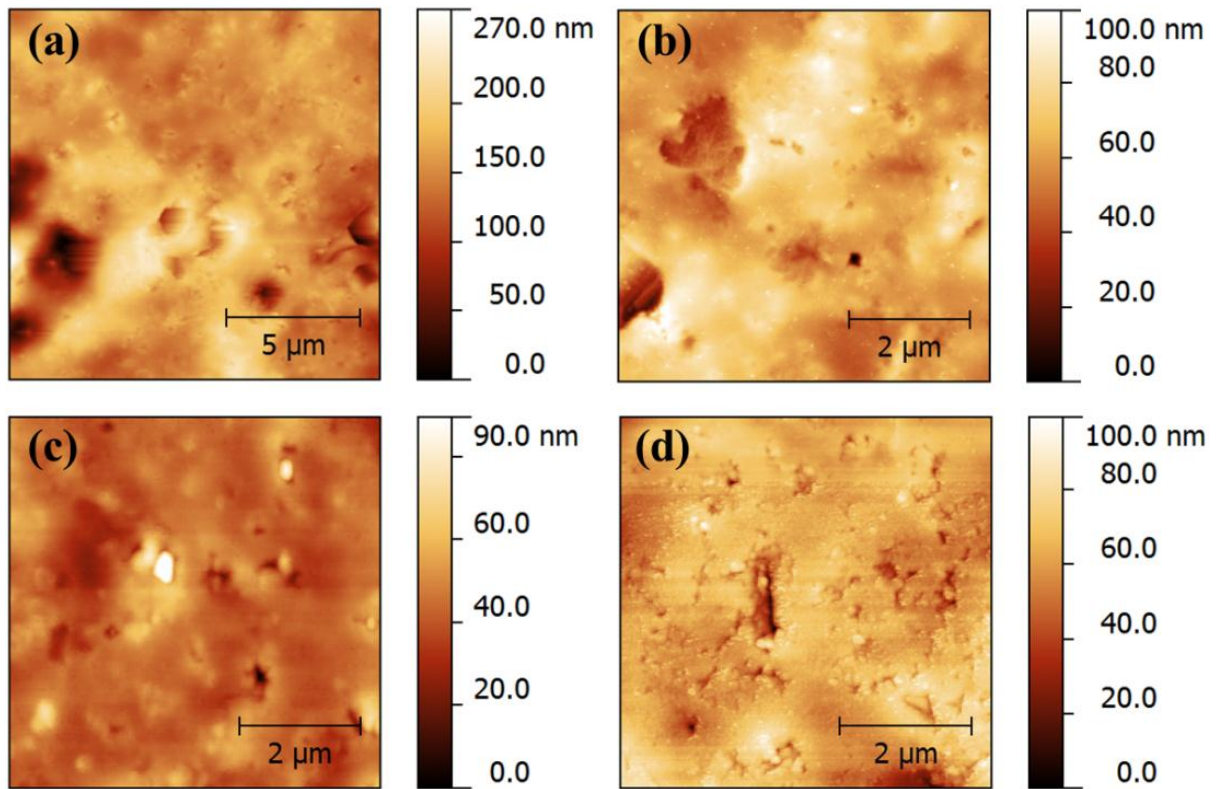


Figure 5.2. AFM surface images of (a) PSR-4000 and PSR-4000 with 100 Al₂O₃ ALD cycles deposited at (b) 60 °C, (c) 90 °C, and (d) 120 °C.

Figure 5.3 shows the phase image of the sample processed under 60 °C. Different color in the phase image was observed when the tapping force was large. The phase image of samples recorded during the AFM test can be used to determine the surface is hard or soft. Bright part on the image means hard sample and dark part represents hard sample. The different color in the phase image means there are some relatively soft spot on the coating. The cause of those soft spots is not known, but they might be related to the voids in the coating that are shown in TEM images.

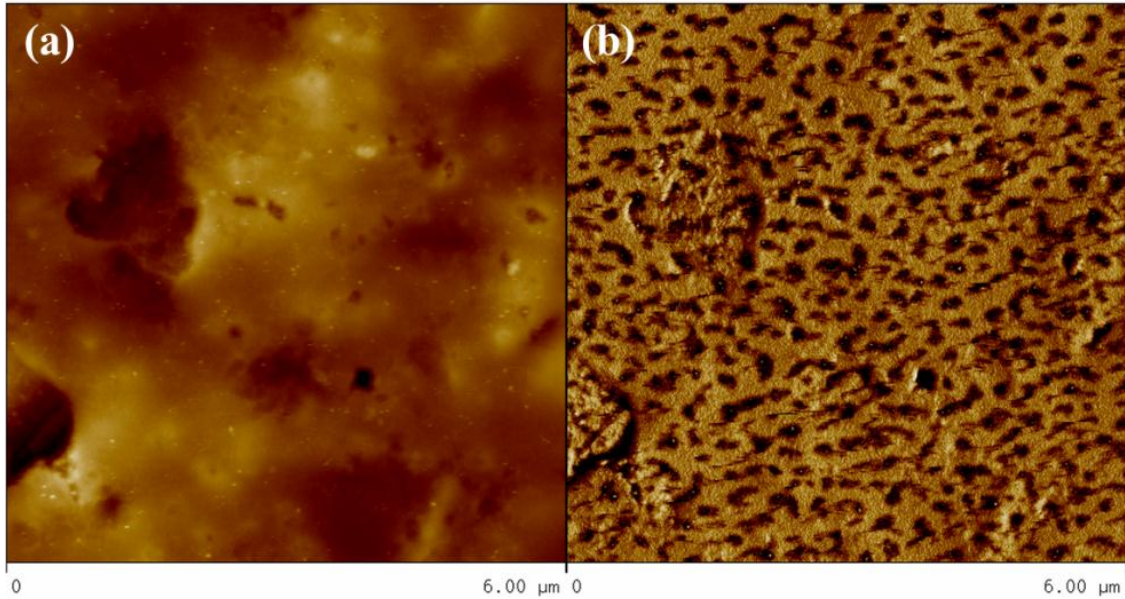


Figure 5.3. (a) AFM height image and (b) AFM phase image of PSR-4000 with 100 Al₂O₃ ALD cycles deposited at 60 °C.

5.3 Mechanical Analysis

Figure 5.4 shows the contact modulus and hardness of different samples. Similar to alumina coatings on PA-6, the contact modulus and hardness shown in figure 5.4 also displays decreasing trends as the applied load increases, which is due to the effect of soft substrate. All PSR-4000 with alumina coatings showed a larger contact modulus and hardness than the virgin PSR-4000. The alumina coating grown at 120 °C gives a lower contact modulus and hardness than the coating grown under 60 and 90 °C. This can be attributed to the different thickness of alumina layer on PSR-4000.

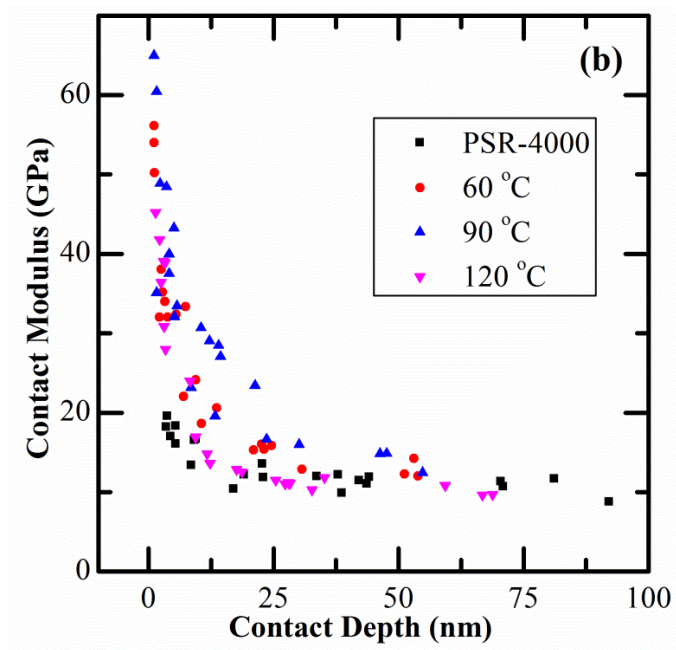
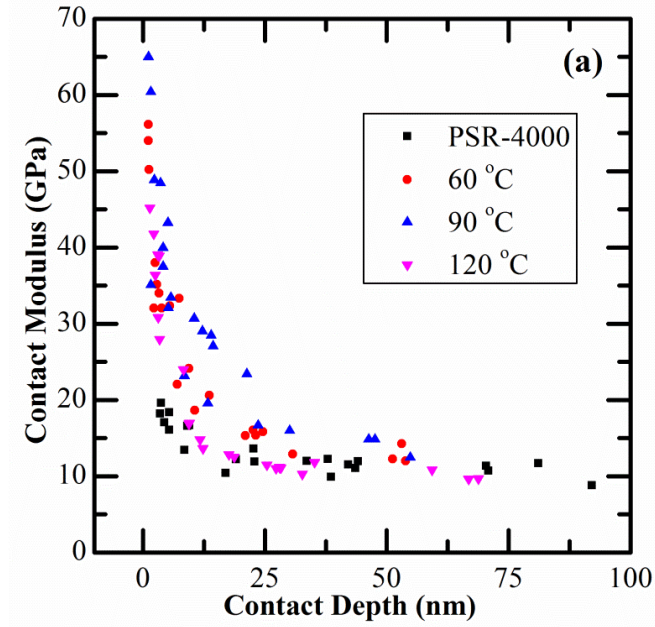


Figure 5.4. Variation of (a) contact modulus and (b) hardness against the contact depth for PSR-4000 and PSR-4000 with 100 cycles ALD alumina coatings grown under 60, 90 and 120 °C.

From the TEM images of PSR-4000, it is noticed that the thickness of alumina layer deposited at 60 and 90 °C are much thicker compared to that deposited at 120°C. The thick coating leads to a smaller substrate effect that could reduce the mechanical properties of the coating dramatically. When the growth temperature is 120 °C, the substrate has the biggest effect on the modulus and hardness of the sample. Thus, the measured results of alumina processed under 120 °C become smaller than the thick alumina coatings grown under 60 and 90 °C, as is less influenced by the substrate.

Flexural test was not performed on the PSR-4000 because the board was not transparent and the cracks happened on the alumina coating couldn't been seen. However, no hybrid layer was formed between the alumina coating and PSR-4000, the critical tensile strain of the coatings can be predicted according to the previous works that have proved a $(1/h)^{1/2}$ dependence for the critical tensile strain where h is the thickness of the coating.[64, 77] Although the difference in the coating caused by different deposition temperature may affect its flexural fracture behavior, the film thickness will be the dominated factor.

5.4 Conclusion

As the composition information of PSR-4000 is not available, the growth mechanism of ALD coating on PSR-4000 cannot be understood. TEM analysis indicates that there is no reaction between the PSR-4000 and ALD alumina. Thick ALD alumina coating was observed on the sample processed under 60 °C and 90 °C, which contains voids in the middle of the layer. The surface of PSR-4000 sheets is very rough and 100 cycles ALD alumina coating is not enough to cover the surface holes. Thick coating is needed to obtain good barrier property.

The alumina coated PSR-4000 show higher modulus and hardness than the uncoated sample. As the coating deposited at 120 °C is much thinner than the other two samples which are processed under 60 and 90 °C, it has a lower elastic modulus and hardness than the other two samples.

6. THESIS SUMMARY

In this study, the growth mechanisms of ALD alumina on PA-6 and PSR-4000 were investigated. The influence of ALD coatings on the surface microstructure of polymers was observed from the AFM and TEM analysis of samples. The mechanical behavior of ALD alumina coatings on polymers was determined in terms of subsurface nucleation of ALD coatings. Overall, it is concluded that the growth behavior of ALD alumina coatings on these polymers affect their resulting mechanical properties.

The primary focus of this work was the growth of ALD alumina on PA-6. This focus was mainly due to what was already known regarding the formation of ALD alumina on PA-6. The reaction between TMA and carbonyl groups of PA-6 allows for a subsurface reaction to form a hybrid interface between the PA-6 and alumina coating. TEM imaging of PA-6 with 100 cycles ALD grown at different temperatures show that the thickness of hybrid layer decreased with an increasing temperature, indicating a prevention of diffusion of TMA into polymers at higher temperature. The prevention is attributed to an increased reaction between TMA and carbonyl groups in the first several cycles, which was enhanced at higher temperature.

In general, the surface microstructure of PA-6 is not altered after ALD processing. Some delamination was observed after processing at 60 °C, attributed to moisture diffusion into the polymer via nano-scale pin holes on the surface of ALD alumina coating.

The elastic modulus and hardness of ALD alumina on PA-6 processed under different temperatures were determined using nanoindentation. The extrapolated values show an

increasing trend with the deposition temperature, which is presumed to be due, in part, to the formation of hybrid layer under the alumina coatings. The hybrid layer behavior also was shown to affect the fracture behavior of alumina coating as it permits efficient transfer of the energy released by cracks formation when a tensile strain is applied. The coating deposited at higher temperatures is observed to have a larger critical tensile strain.

The PSR-4000 is a commercial polymer, of proprietary composition, that is common in flexible printed circuit boards. TEM analysis indicated no diffusion of precursors into the polymer during processing and therefore no formation of an underlying hybrid layer. Still, the thickness of the ALD coating deposited at different temperatures varied. The surface of the PSR-4000 board was very rough, even after the coating of alumina, as observed by the presence of holes on the surface. These defects suggest routes for moisture penetration into the polymer.

The mechanical properties of PSR-4000 with alumina coatings were investigated using nanoindentation. As the thickness of alumina coating grown at 120 °C was much smaller compared to the coatings deposited at 60 and 90 °C, the substrate effect was larger for the coating. Therefore, the elastic modulus and hardness of alumina obtained at 120 °C were both smaller than those processed at 60 and 90 °C.

In summary, the growth mechanisms of alumina ALD on PA-6 and its effects on the surface microstructure of PA-6 were investigated. The mechanical behavior of ALD alumina coatings on PA-6 in terms of the structure of the coating/substrate system was determined. In addition, the growth and mechanical behavior of ALD alumina on PSR-4000 were observed.

7. FUTURE WORK

Three directions for future work are proposed:

- 1) While this study examined the mechanical and crack formation properties of ALD coatings, the influence of these characteristics on the barrier properties of the coating needs to be investigated. The next logical step is to measure the water vapor transmission rate of these samples to observe the influence of the hybrid layer on the barrier properties.
- 2) From the result of bending test, it is obvious that the critical tensile strain of the ALD alumina coating on PA-6 increases with the deposition temperature, but the initiated crack density is larger. A better temperature might exist at which the critical tensile strain of the coating is large enough to make sure the coating has the required flexibility while the initiated crack density remains small. Additional testing is needed to examine a broader deposition temperature range to find this optimum condition.
- 3) It is proposed that a low temperature hybrid layer followed by a high temperature ALD coating may result in enhanced flexibility. In this architecture, the hybrid coating slow down the crack formation during the flexing test and the high temperature coatings would have a higher critical tensile strain. If the hybrid layer and high temperature ALD coating can be combined together, the flexibility of the ALD coating might be improved.

8. REFERENCES

1. Lewis, J., *Material Challenge for Flexible Organic Devices*. Materials Today, 2006. **9**(4): p. 38-45.
2. Park, J., Chae, H., Chung, H.K. and Lee, S.I., *Thin Film Encapsulation for Flexible AM-OLED: a Review*. Semiconductor Science and Technology, 2011. **26**(3).
3. Puurunen, R.L., *Surface Chemistry of Atomic Layer Deposition: A Case Study for the Trimethylaluminum/water Process*. Journal of Applied Physics, 2005. **97**(12).
4. Groner, M.D., Fabreguette, F.H., Elam, J.W. and George, S.M., *Low-temperature Al₂O₃ Atomic Layer Deposition*. Chemistry of Materials, 2004. **16**(4): p. 639-645.
5. George, S.M., *Atomic Layer Deposition: An Overview*. Chemical Reviews, 2010. **110**(1): p. 111-131.
6. Suntola, T.a.H., J., *Atomic Layer Epitaxy*. Annual Review of Materials Science, 1985. **15**: p. 177-195.
7. Finch, D.S., Oreskovic, T., Ramadurai, K., Herrmann, C.F., George, S.M. and Mahajan, R.L., *Biocompatibility of Atomic Layer-deposited Alumina Thin Films*. Journal of Biomedical Materials Research Part A, 2008. **87A**(1): p. 100-106.
8. Hirvikorpi, T., Vaha-Nissi, M., Harlin, A., Salomaki, M., Areva, S., Korhonen, J.T. and Karppinen, M., *Enhanced Water Vapor Barrier Properties for Biopolymer Films by Polyelectrolyte Multilayer and Atomic Layer Deposited Al₂O₃ Double-coating*. Applied Surface Science, 2011. **257**(22): p. 9451-9454.
9. Ritala, M.a.L., M., *Atomic Layer Deposition*, in *Handbook of Thin Film Materials*, H.S. Nalwa, Editor. 2002, Academic Press: San Diego. p. 103-159.
10. Hirvikorpi, T., Vaha-Nissi, M., Mustonen, T., Iiskola, E. and Karppinen, M., *Atomic Layer Deposited Aluminum Oxide Barrier Coatings for Packaging Materials*. Thin Solid Films, 2010. **518**(10): p. 2654-2658.
11. Spagnola, J.C., Gong, B., Arvidson, S.A., Jur, J.S., Khan, S.A. and Parsons, G.N., *Surface and Sub-surface Reactions during Low Temperature Aluminium Oxide Atomic Layer Deposition on Fiber-forming Polymers*. Journal of Materials Chemistry, 2010. **20**(20): p. 4213-4222.
12. Jur, J.S., Spagnola, J.C., Lee, K., Gong, B., Peng, Q. and Parsons, G.N., *Temperature-Dependent Subsurface Growth during Atomic Layer Deposition on Polypropylene and Cellulose Fibers*. Langmuir, 2010. **26**(11): p. 8239-8244.

13. Tripp, M.K., Stampfer, C., Miller, D.C., Helbling, T., Hermann, C.F., Hierold, C., Gall, K., George, S.M. and Bright, V.M., *The Mechanical Properties of Atomic Layer Deposited Alumina for Use in Micro- and Nano-electromechanical Systems*. Sensors and Actuators a-Physical, 2006. **130**: p. 419-429.
14. Tapily, K., Jakes, J.E., Stone, D.S., Shrestha, P., Gu, D., Baumgart, H. and Elmustafa, A.A., *Nanoindentation Investigation of HfO₂ and Al₂O₃ Films Grown by Atomic Layer Deposition*. Journal of the Electrochemical Society, 2008. **155**(7): p. H545-H551.
15. Miller, D.C., Foster, R.R., Jen, S.H., Bertrand, J.A., Cunningham, S.J., Morris, A.S., Lee, Y.C., George, S.M. and Dunn, M.L., *Thermo-mechanical Properties of Alumina Films Created Using the Atomic Layer Deposition Technique*. Sensors and Actuators a-Physical, 2010. **164**(1-2): p. 58-67.
16. Oliver, W.C.a.P., G.M., *An Improved Technique for Determining Hardness and Elastic-Modulus Using Load and Displacement Sensing Indentation Experiments*. Journal of Materials Research, 1992. **7**(6): p. 1564-1583.
17. Saha, R.a.N., W.D., *Effects of the Substrate on the Determination of Thin Film Mechanical Properties by Nanoindentation*. Acta Materialia, 2002. **50**(1): p. 23-38.
18. Bull, S.J., *Mechanical Response of Atomic Layer Deposition Alumina Coatings on Stiff and Compliant Substrates*. Journal of Vacuum Science & Technology A, 2012. **30**(1).
19. Dillon, A.C., Ott, A.W., Way, J.D. and George, S.M., *Surface-Chemistry of Al₂O₃ Deposition Using Al(CH₃)₃ and H₂O in a Binary Reaction Sequence*. Surface Science, 1995. **322**(1-3): p. 230-242.
20. Kemell, M., Farm, E., Ritala, M. and Leskela, M., *Surface Modification of Thermoplastics by Atomic Layer Deposition of Al₂O₃ and TiO₂ Thin Films*. European Polymer Journal, 2008. **44**(11): p. 3564-3570.
21. Narayan, R.J., Adiga, S.P., Pellin, M.J., Curtiss, L.A., Hryn, A.J., Stafslie, S., Chisholm, B., Shih, C., Shih, C., Lin, S., Su, Y., Jin, C., Zhang, J., Monteiro-Riviere, N.A. and Elam, J.W., *Atomic Layer Deposition-based Functionalization of Materials for Medical and Environmental Health Applications*. Philosophical Transactions of the Royal Society a-Mathematical Physical and Engineering Sciences, 2010. **368**(1917): p. 2033-2064.
22. Hyde, G.K., Scarel, G., Spagnola, J.C., Peng, Q., Lee, K., Gong, B., Roberts, K.G., Roth, K.M., Hanson, C.A., Devine, C.K., Stewart, S.M., Hojo, D., Na, J.S., Jur, J.S. and Parsons, G.N., *Atomic Layer Deposition and Abrupt Wetting Transitions on*

- Nonwoven Polypropylene and Woven Cotton Fabrics*. Langmuir, 2010. **26**(4): p. 2550-2558.
23. Carcia, P.F., McLean, R.S., Reilly, M.H., Groner, M.D. and George, S.M., *Ca Test of Al₂O₃ Gas Diffusion Barriers Grown by Atomic Layer Deposition on Polymers*. Applied Physics Letters, 2006. **89**(3).
 24. Dameron, A.A., Davidson, S.D., Burton, B.B., Carcia, P.F., McLean, R.S. and George, S.M., *Gas Diffusion Barriers on Polymers Using Multilayers Fabricated by Al₂O₃ and Rapid SiO₂ Atomic Layer Deposition*. Journal of Physical Chemistry C, 2008. **112**(12): p. 4573-4580.
 25. Carcia, P.F., McLean, R.S., Groner, M.D., Dameron, A.A. and George, S.M., *Gas Diffusion Ultrabarrriers on Polymer Substrates Using Al₂O₃ Atomic Layer Deposition and SiN Plasma-enhanced Chemical Vapor Deposition*. Journal of Applied Physics, 2009. **106**(2).
 26. Ritala, M., Leskela, M., Niinisto, L., Prohaska, T., Friedbacher, G. and Grasserbauer, M., *Development of Crystallinity and Morphology in Hafnium Dioxide Thin-Films Grown by Atomic Layer Epitaxy*. Thin Solid Films, 1994. **250**(1-2): p. 72-80.
 27. Ritala, M., Leskela, M., Nykanen, E., Soininen, P. and Niinisto, L., *Growth of Titanium-Dioxide Thin-Films by Atomic Layer Epitaxy*. Thin Solid Films, 1993. **225**(1-2): p. 288-295.
 28. Yamada, A., Sang, B.S. and Konagai, M., *Atomic Layer Deposition of ZnO Transparent Conducting Oxides*. Applied Surface Science, 1997. **112**: p. 216-222.
 29. Kukli, K., Ritala, M., Leskela, M. and Jokinen, J., *Atomic Layer Epitaxy Growth of Aluminum Oxide Thin Films From a Novel Al(CH₃)₂Cl Precursor and H₂O*. Journal of Vacuum Science & Technology a-Vacuum Surfaces and Films, 1997. **15**(4): p. 2214-2218.
 30. Ott, A.W., McCarley, K.C., Klaus, J.W., Way, J.D. and George, S.M., *Atomic Layer Controlled Deposition of Al₂O₃ Films Using Binary Reaction Sequence Chemistry*. Applied Surface Science, 1996. **107**: p. 128-136.
 31. Ott, A.W., Klaus, J.W., Johnson, J.M. and George, S.M., *Al₂O₃ Thin Film Growth on Si(100) Using Binary Reaction Sequence Chemistry*. Thin Solid Films, 1997. **292**(1-2): p. 135-144.
 32. Higashi, G.S.a.F., C.G., *Sequential Surface Chemical-Reaction Limited Growth of High-Quality Al₂O₃ Dielectrics*. Applied Physics Letters, 1989. **55**(19): p. 1963-1965.

33. Yun, S.J., Lee, K.H., Skarp, J., Kim, H.R. and Nam, K.S., *Dependence of Atomic Layer-Deposited Al₂O₃ Films Characteristics on Growth Temperature and Al Precursors of Al(CH₃)₃ and AlCl₃*. Journal of Vacuum Science & Technology - Vacuum Surfaces and Films, 1997. **15**(6): p. 2993-2997.
34. Kim, E.H., Lee, D.H., Chung, B.H., Kim, H.S., Kim, Y. and Noh, S.J., *Low-Temperature Growth of ZnO Thin Films by Atomic Layer Deposition*. Journal of the Korean Physical Society, 2007. **50**(6): p. 1716-1718.
35. Kim, H., *Atomic Layer Deposition of Metal and Nitride Thin Films: Current Research Efforts and Applications for Semiconductor Device Processing*. Journal of Vacuum Science & Technology B, 2003. **21**(6): p. 2231-2261.
36. Kim, H.a.R., S.M., *Plasma-enhanced Atomic Layer Deposition of Tantalum Thin Films: the Growth and Film Properties*. Thin Solid Films, 2003. **441**(1-2): p. 311-316.
37. Kwon, O.K., Kwon, S.H., Park, H.S. and Kang, S.W., *Plasma-Enhanced Atomic Layer Deposition of Ruthenium Thin Films*. Electrochemical and Solid-State Letters, 2004. **7**(4): p. C46.
38. Lee, H.B.R.a.K., H., *High-Quality Cobalt Thin Films by Plasma-Enhanced Atomic Layer Deposition*. Electrochemical and Solid-State Letters, 2006. **9**(11): p. G323.
39. Kim, H., Cabral, C., Lavoie, C. and Rossnagel, S.M., *Diffusion Barrier Properties of Transition Metal Thin Films Grown by Plasma-enhanced Atomic Layer Deposition*. Journal of Vacuum Science & Technology B, 2002. **20**(4): p. 1321-1326.
40. Heil, S.B.S., Kudlacek, P., Langereis, E., Engeln, R., Van de Sanden, M.C.M. and Kessels, W.M.M., *In Situ Reaction Mechanism Studies of Plasma-assisted Atomic Layer Deposition of Al₂O₃*. Applied Physics Letters, 2006. **89**(13).
41. Langereis, E., Creatore, M., Heil, S.B.S., Van de Sanden, M.C.M. and Kessels, W.M.M., *Plasma-assisted Atomic Layer Deposition of Al₂O₃ Moisture Permeation Barriers on Polymers*. Applied Physics Letters, 2006. **89**(8).
42. Seshan, K., *Handbook of Thin-Film Deposition Processes and Techniques - Principles, Methods, Equipment and Applications (2nd Edition)*. 2002, William Andrew Publishing/Noyes. p. 11-43.
43. Xu, Y.a.M., C.B., *A DFT Study of the Al₂O₃ Atomic Layer Deposition on SAMs: Effect of SAM Termination*. Chemistry of Materials, 2004. **16**(4): p. 646-653.
44. Wilson, C.A., Grubbs, R.K. and George, S.M., *Nucleation and Growth During Al₂O₃ Atomic Layer Deposition on Polymers*. Chemistry of Materials, 2005. **17**(23): p. 5625-5634.

45. Yousfi, E.B., Fouache, J. and Lincot, D., *Study of Atomic Layer Epitaxy of Zinc Oxide by In-situ Quartz Crystal Microgravimetry*. Applied Surface Science, 2000. **153**(4): p. 223-234.
46. Weaver, M.S., Michalski, L.A., Rajan, K., Rothman, M.A., Silvernail, J.A., Brown, J.J., Burrows, P.E., Graff, G.L., Gross, M.E., Martin, P.M., Hall, M., Mast, E., Bonham, C., Bennett, W. and Zumhoff, M., *Organic Light-emitting Devices with Extended Operating Lifetimes on Plastic Substrates*. Applied Physics Letters, 2002. **81**(16): p. 2929-2931.
47. Lewis, J.S.a.W., M.S., *Thin-film Permeation-barrier Technology for Flexible Organic Light-emitting Devices*. Ieee Journal of Selected Topics in Quantum Electronics, 2004. **10**(1): p. 45-57.
48. Groner, M.D., George, S.M., McLean, R.S. and Carcia, P.F., *Gas Diffusion Barriers on Polymers Using Al₂O₃ Atomic Layer Deposition*. Applied Physics Letters, 2006. **88**(5).
49. Spagnola, J.C., Gong, B. and Parsons, G.N., *Surface Texture and Wetting Stability of Polydimethylsiloxane Coated with Aluminum Oxide at Low Temperature by Atomic Layer Deposition*. Journal of Vacuum Science & Technology A, 2010. **28**(6): p. 1330-1337.
50. Hyde, G.K., McCullen, S.D., Jeon, S., Stewart, S.M., Jeon, H., Lobo, E.G. and Parsons, G.N., *Atomic Layer Deposition and Biocompatibility of Titanium Nitride Nano-coatings on Cellulose Fiber Substrates*. Biomedical Materials, 2009. **4**(2).
51. Peng, Q., Sun, X.Y., Spagnola, J.C., Hyde, G.K., Spontak, R.J. and Parsons, G.N., *Atomic Layer Deposition on Electrospun Polymer Fibers as a Direct Route to Al₂O₃ Microtubes with Precise Wall Thickness Control*. Nano Letters, 2007. **7**(3): p. 719-722.
52. Fabreguette, F.H.a.G., S.M., *X-ray Mirrors on Flexible Polymer Substrates Fabricated by Atomic Layer Deposition*. Thin Solid Films, 2007. **515**(18): p. 7177-7180.
53. Orefice, R.L.a.B., A., *Controlled Modification of the Structure of Polymer Surfaces by Chemically Grafting Inorganic Species*. materials Research, 1999. **2**(3): p. 153-157.
54. Low, H.a.X., Y.G., *Moisture Barrier of Al_xO_y Coating on Poly(ethylene terephthalate), Poly(ethylene naphthalate) and Poly(carbonate) Substrates*. Applied Surface Science, 2005. **250**(1-4): p. 135-145.

55. Gross, D., *Fracture Mechanics: With an Introduction to Micromechanics*. 2nd ed. 2011, New York: Springer.
56. Pompe, W., Bobeth, M., Hollatz, R., Krawietz, R., Romanov, A. and Ullrich, A., *Fracture Mechanisms and Strength of Thin Films*. *Advances in Solid State Physics*, 1999. **39**: p. 551-560.
57. *Fracture Mechanics*. Available from: http://en.wikipedia.org/wiki/Fracture_mechanics.
58. Yanaka, M., Tsukahara, Y., Nakaso, N. and Takeda, N., *Cracking Phenomena of Brittle Films in Nanostructure Composites Analysed by a Modified Shear Lag Model with Residual Strain*. *Journal of Materials Science*, 1998. **33**(8): p. 2111-2119.
59. *Fracture Toughness*. Available from: http://en.wikipedia.org/wiki/Fracture_toughness.
60. Beuth, J.L., *Cracking of Thin Bonded Films in Residual Tension*. *International Journal of Solids and Structures*, 1992. **29**(13): p. 1657-1675.
61. Mohanty, B.C., Choi, H.R., Choi, Y.M. and Cho, Y.S., *Thickness-dependent Fracture Behaviour of Flexible ZnO:Al Thin Films*. *Journal of Physics D: Applied Physics*, 2011. **44**(2).
62. Fischer-Cripps, A.C., *Nanoindentation*. 2nd ed. 1994, New York: Springer.
63. ISO14577-4, *Test method for metallic and non-metallic coatings, in Metallic materials -- Instrumented indentation test for hardness and materials parameters*. 2007.
64. Jen, S., Bertrand, J.A. and George, S.M., *Critical Tensile and Compressive Strains for Cracking of Al₂O₃ Films Grown by Atomic Layer Deposition*. *Journal of Applied Physics*, 2011. **109**(8).
65. Miller, D.C., Foster, R.R., Zhang, Y., Jen, S., Bertrand, J.A., Lu, Z., Seghete, D., O'Patchen, J.L., Yang, R., Lee, Y., George, S.M. and Dunn, M.L., *The Mechanical Robustness of Atomic-layer- and Molecular-layer-deposited Coatings on Polymer Substrates*. *Journal of Applied Physics*, 2009. **105**(9).
66. Zhang, Y.D., Yang, R.G., George, S.M. and Lee, Y.C., *In-situ Inspection of Cracking in Atomic-layer-deposited Barrier Films on Surface and in Buried Structures*. *Thin Solid Films*, 2011. **520**(1): p. 251-257.
67. Latella, B.A., Triani, G. and Evans, P.J., *Toughness and Adhesion of Atomic Layer Deposited Alumina Films on Polycarbonate Substrates*. *Scripta Materialia*, 2007. **56**(6): p. 493-496.

68. Thurn, J.a.C., R.F., *Mechanical and Thermal Properties of Physical Vapour Deposited Alumina Films - Part II - Elastic, Plastic, Fracture, and Adhesive Behaviour*. Journal of Materials Science, 2004. **39**(15): p. 4809-4819.
69. Casellas, D., Nagl, M.M., Llanes, L. and Anglada, A., *Fracture Toughness of Alumina and ZTA Ceramics: Microstructural Coarsening Effects*. Journal of Materials Processing Technology, 2003. **143**: p. 148-152.
70. Accuratus. *Aluminum Oxide, Al₂O₃ Material Characteristics*. Available from: <http://accuratus.com/alumox.html>.
71. Venkatachalam, D.K., Bradby, J.E., Saleh, M.N., Ruffell, S. and Elliman, R.G., *Nanomechanical Properties of Sputter-deposited HfO₂ and Hf_xSi_{1-x}O₂ Thin Films*. Journal of Applied Physics, 2011. **110**(4).
72. *Transmission Electron Microscopy*.
73. Chatterjee, S., Gadad, S.S. and Kundu, T.K., *Atomic Force Microscopy*. Resonance, 2010. **15**(7): p. 622-642.
74. Coupeau, C., *Atomic Force Microscopy Study of the Morphological Shape of Thin Film Buckling*. Thin Solid Films, 2002. **406**(1-2): p. 190-194.
75. Jian, S.R., Chen, G.J. and Lin, T.C., *Berkovich Nanoindentation on AlN Thin Films*. Nanoscale Research Letters, 2010. **5**(6): p. 935-940.
76. Lee, W.S.a.F., F.J., *Microstructural Study of Annealed Gold–silicon Thin Films under Nanoindentation*. Materials Science and Engineering: A, 2008. **475**(1-2): p. 319-326.
77. Leterrier, Y., *Durability of Nanosized Oxygen-barrier Coatings on Polymers - Internal Stresses*. Progress in Materials Science, 2003. **48**(1): p. 1-55.